Local Cation Order and Ferrimagnetism in Compositionally Complex Spinel Ferrites

Xin Wang, Brianna Musicó, Corisa Kons, Peter Metz, Veerle Keppens, and Dustin A. Gilbert
Department of Materials Science and Engineering,
University of Tennessee, Knoxville, Tennessee 37996 USA.

Yuanpeng Zhang
Neutron Scattering Division, Oak Ridge National
Laboratory, Oak Ridge, Tennessee 37831 USA.

Katharine Page*
Department of Materials Science and Engineering,
University of Tennessee, Knoxville, Tennessee 37996 USA.
Neutron Scattering Division, Oak Ridge National
Laboratory, Oak Ridge, Tennessee 37831 USA. and
Shull Wollan Center, Oak Ridge National Laboratory, Oak Ridge, Tennessee 37831 USA.

(Dated: October 10, 2022)

Abstract

We present an exploration of a family of compositionally complex cubic spinel ferrites featuring combinations of Mg, Fe, Co, Ni, Cu, Mn, and Zn cations, systematically investigating the average and local atomic structure, chemical short-range order, magnetic spin configurations, and magnetic properties. All compositions result in ferrimagnetic average structures with extremely similar local bonding environments, however the samples display varying degrees of cation inversion and therefore differing apparent bulk magnetization. Additionally, first-order reversal curve (FORC) analysis of the magnetic reversal behavior indicates varying degrees of magnetic ordering and interactions, including potentially local frustration. Finally, reverse Monte Carlo (RMC) modeling of the spin orientation demonstrates a relationship between the degree of cation inversion and the spin collinearity. Collectively, these observations correlate with differences in synthesis procedures. This work provides a framework for understanding magnetic behavior reported for "high-entropy spinels," revealing many are likely compositionally complex oxides with differing degrees of chemical short-range order– not meeting the community established criteria for high or medium entropy compounds. Moreover, this work highlights the importance of reporting complete sample processing histories and investigating local to long-range atomic arrangements when evaluating potential entropic mixing effects and assumed property correlations in high entropy materials.

I. INTRODUCTION

High entropy oxides (HEOs) are being increasingly reported in various oxide crystal structures, including in the perovskite, fluorite, spinel and pyrochlore structure motifs [1–18]. HEOs are generally described as single phase solid solution systems exhibiting five or more homogeneously distributed cations in equimolar or near-equimolar ratios on a single crystallographic site. When a positive entropy of formation (ΔS_f) overcomes a positive enthalpy of formation (ΔH_f), the Gibbs free energy of formation ($\Delta G_f = \Delta H_f - T\Delta S_f$) will be negative, making the system an entropy stabilized oxide (ESO). The ESO, a five component oxide ($(Mg_{0.2}Ni_{0.2}Co_{0.2}Cu_{0.2}Zn_{0.2})O$), exhibiting a single rock salt phase, was first introduced by Rost *et al.* in 2015 [19]. HEOs/ESOs draw interest due to inherent opportunities to tailor and combine materials properties. The extent to which their enhanced

---

* kpage10@utk.edu

compositional and configurational complexity impart additional stability, synergistic effects, and emergent/tunable properties to HEO archetypes is an active area of exploration. The magnetic properties of HEOs represent one of the fastest growing research directions in this scientific community. From the perspective of magnetic behavior, the complexity of the local and long-range nuclear and spin structures found in HEOs gives rise to an unusually large number of metal-oxygen-metal interactions[20]. The inherent variation in coordination geometry, valence state, spin state, number of cations and metal cation type each HEO lattice can accommodate presents a rich pallet for exploring the tunability of the structure-property effects in the class. However, relatively few compositions have been studied in detail[20], no doubt due in part to the complex cation and spin order likely to be present.

Spinels crystallizing in cubic space group $Fd\bar{3}m$, with nominal formula AB_2O_4, feature a close-packed oxygen substructure with two thirds of cations occupying octahedral interstices and one third occupying tetrahedral ones. The spinel compounds in this work involve A and B cations in the cation charge state combination of +2 and +3 (charge-balanced spinel oxide families with +2 and +1, and +6 and +1 cation combinations are also known to exist). Spinels are typically classified according to which cations occupy the respective coordination environments, with a degree of inversion, γ, denoting the fraction of A ions occupying the octahedral sites, $[A_{1-\gamma}B_\gamma]_{tet}[A_\gamma B_{2-\gamma}]_{oct}O_4$. In the “normal” spinel structure ($\gamma = 0$, $[A]_{tet}[B_2]_{oct}O_4$), B^{3+} fully occupies the spinel octahedral site, while A^{2+} fully occupies the tetrahedral site. In the “inverse” spinel structure ($\gamma = 1$, $[B]_{tet}[AB]_{oct}O_4$), half of the B^{3+} cations fully occupy the tetrahedral site, leaving an equal amount of A^{2+} and B^{3+} atoms occupying the octahedral site. In a “random” spinel structure ($\gamma = 2/3$, $[A_{1/3}B_{2/3}]_{tet}[A_{2/3}B_{4/3}]_{oct}O_4$), A^{2+} and B^{3+} atoms take up residence on both sites according to their overall molar ratio, with 1/3 and 2/3 distribution, respectively. Arbitrary intermediate states between the normal and inverse spinels are possible (γ value between 0 and 1). FIG. 1 provides a depiction of high entropy spinel AB_2O_4 (with A = 5 equimolar cations and B = a single metal cation), shown for the case of the inverse spinel ferrite structure.

Specific (not random) cation site preferences of the crystal chemistry in spinel oxides are well documented in the literature[21, 22], going back to early reports[23, 24] linking cation site distribution and magnetic properties in spinel ferrites. There has been ample research into the magnetic properties of spinel AFe_2O_4 since. AFe_2O_4 (A = Fe^{2+}[25, 26], Ni^{2+}[27], Cu^{2+}[28], Mg^{2+}[29], or Co^{2+}[26, 30, 31]) spinels have a variety of important applications in

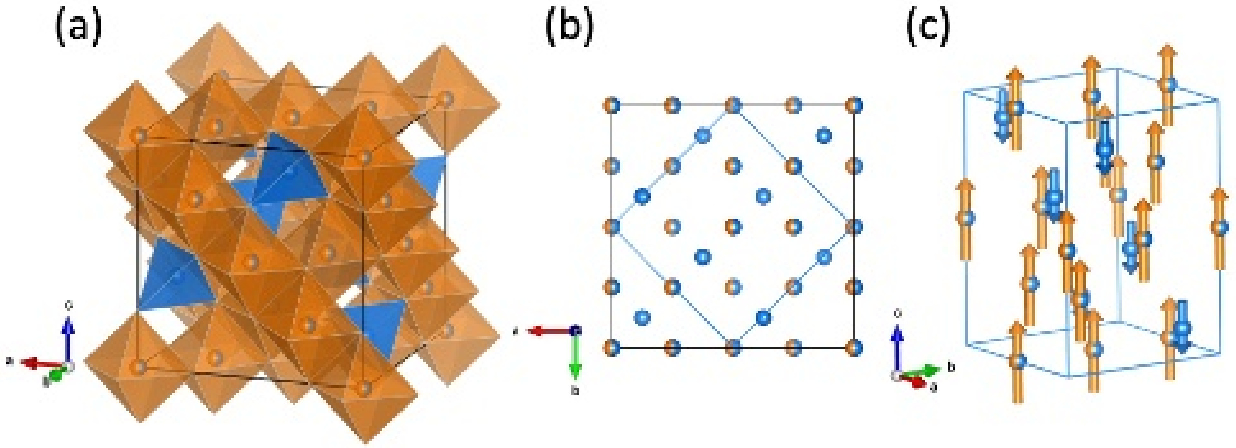

FIG. 1. Schematic view of (a) the inverse spinel unit cell with blue tetrahedra (A-sites) and orange octahedra (B-sites). Cations on the octahedral site are drawn half blue and half orange to represent site mixing. Oxygen atoms sitting on polyhedral vertices are omitted for clarity. (b) The [0 0 1] projection of the cation substructure in the unit cell (black square) overlaid with the unit cell of the magnetic structure (blue frame). (c) The room-temperature zero-field magnetic spin structure composed of magnetic moments on the tetrahetral site (blue vectors pointing down) and octahedral site (orange vectors pointing up).

magnetic technologies[24, 32, 33]. They all have an inverse (either partially or completely) spinel structure. Previous works have shown that, in spinel ferrites, Zn^{2+} prefers to occupy the tetrahedral site while Mg^{2+}, Mn^{2+}, Mn^{3+}, Fe^{2+}, Fe^{3+}, Ni^{2+}, Cu^{2+}, and Co^{2+} tend to occupy the octahedral site in spinel ferrites[24]. It remains to be seen whether high entropy spinels will follow the trends in site preference observed among the ternary spinel ferrite

Year	Chem.	GS	Ref.
Solid State Method + Sintering			
2019	$(Mg_{0.2}M_{0.2}Co_{0.2}Ni_{0.2}Cu_{0.2})Fe_2O_4$, M=Zn,Mn,Fe	FIM	[35]
2019	$(Mn_{0.2}Fe_{0.2}Co_{0.2}Ni_{0.2}Cu_{0.2})Fe_2O_4$	FIM	[35]
2020	$(Co_{0.2}Mn_{0.2}Ni_{0.2}Fe_{0.2}Zn_{0.2})Fe_2O_4$ (no sintering)	N/A	[46]
2022	$(Mg_{0.2}Fe_{0.2}Co_{0.2}Ni_{0.2}M_{0.2})Fe_2O_4$, M=Mn,Cu,Zn	FIM	[49]
Co-Precipitation + Annealing			
2019	$(Zn_{0.2}Mg_{0.2}Ni_{0.2}Fe_{0.2}Cd_{0.2})Fe_2O_4$	N/A	[50]
Sol-Gel Method			
2020	$(Co_{0.2}Cr_{0.2}Fe_{0.2}Mn_{0.2}Ni_{0.2})Fe_2O_4$	FIM	[60]
Solution Combustion Synthesis (SCS)			
2021	$(MnNiCuZn)_{1-x}Co_xFe_2O_4$ (x=0.05,0.1,0.2,0.3)	FIM	[58]
Glycine-Combustion Method			
2022	$(M_{0.2}Zn_{0.2}Co_{0.2}Ni_{0.2}Cu_{0.2})Fe_2O_4$, M=Mn,Fe	N/A	[67]
2022	$(Mn_{0.2}Fe_{0.2}Co_{0.2}Ni_{0.2}Cu_{0.2})Fe_2O_4$	N/A	[67]

TABLE I. A summary of powder sample high entropy spinel ferrite compositions appearing in the literature, including year reported (Year), chemical composition (Chem.), magnetic ground state (GS) (where FIM denotes ferrimagnetic), and the reference (Ref.).

systems, or if the potential for increased configurational entropy will lead to more random cation distributions.

High entropy spinels have been synthesized by solid state[34–49], co-precipitation[50, 51], solution combustion synthesis (SCS)[52–59], sol-gel method[60, 61], solvothermal synthesis[62], reverse co-precipitation[63], flame spray pyrolysis[64], hydrothermal method[65], polymerized complex method[66] and glycine-combustion method[67] among other techniques. Examples of reported high-entropy ferrite powders are summarized in TABLE I.

Research into the magnetic properties and cation site ordering among high entropy spinels is still in its infancy. There is one recent report[68] demonstrating that the site ordering

$(Co_{0.6}Fe_{0.4})(Cr_{0.3}Fe_{0.1}Mn_{0.3}Ni_{0.3})_2O_4$ in A_3O_4 spinel is governed by maximization of the crystal field stabilization energy (CFSE) of the constituent ions through site selectivity rather than by maximization of the configurational entropy (S_{config}) through random and homogenous cation disorder[68]. It is not known whether this generalizes to other high entropy spinel compositions, including compositional variations of the technologically important spinel ferrite (AFe_2O_4). The magnetic properties of spinel ferrites are highly sensitive to the distribution of cations (the degree of inversion, γ) across the tetrahedral and octahedral sublattices [69, 70]. For example, this phenomena has been well explored by mixing of Zn-ferrite (a normal spinel) with Co-ferrite (an inverse spinel), resulting in non-magnetic Zn^{2+} swapping for magnetic Fe^{3+} on octahedral sites and increasing the overall magnetization[71, 72]. Similar effects may arise in compositionally complex spinel samples, potentially with greater sublattice disorder and/or expanded substitution limits for specific cations.

In 2019, Musicó et al. [35] reported on the magnetic properties and trends amongst a series of high entropy spinel ferrites (compositions AFe_2O_4) and chromates (compositions ACr_2O_4). All reported high entropy spinel ferrites were shown to be room temperature ferrimagnets and like several other HEO magnetic phases, were reported to generally follow trends found in the majority of the simpler ternary systems involving groups of the constituent cations. For example, the high entropy system including Zn and Mg (the two non-magnetic cations) had the largest magnetic moment and lowest Néel temperature (T_N) relative to other high entropy spinels. On the other hand, several other HEO ferrites ($(Mg_{0.2}Fe_{0.2}Co_{0.2}Ni_{0.2}Cu_{0.2})Fe_2O_4$ and $(Mg_{0.2}Mn_{0.2}Co_{0.2}Ni_{0.2}Cu_{0.2})Fe_2O_4$) were noted to show peculiar magnetic behavior. For example, the low temperature field warming magnetization dips below the field cooling magnetization and for intermediate temperatures indicates an increase in magnetization as temperature is raised. A possible explanation for this peculiar thermal hysteresis is the antiferromagnetic coupling between neighboring elemental components in the cation sublattice. This leads to a key question of whether the reported high entropy spinels contain cation short-range order and small locally ordered magnetic clusters or chemically homogeneous distributions with more dilute clusters, and whether the substructures can be tuned.

The extent to which high entropy spinels will exhibit cation distributions different from bulk ternary spinels that influence their properties remains to be determined. In this work, we explore the influence of local cation ordering upon magnetic properties in a family

Name	Composition	Heat treatment	
		No.1	No.2
F1	$(Mg_{0.2}Fe_{0.2}Co_{0.2}Ni_{0.2}Cu_{0.2})Fe_2O_4$	1250°C, 10h	1250°C, 10h
F3	$(Mg_{0.2}Co_{0.2}Ni_{0.2}Cu_{0.2}Zn_{0.2})Fe_2O_4$	1250°C, 10h	1250°C, 10h
F4	$(Mg_{0.2}Mn_{0.2}Co_{0.2}Ni_{0.2}Cu_{0.2})Fe_2O_4$	950°C, 10h	1250°C, 10h
F5	$(Mn_{0.2}Fe_{0.2}Co_{0.2}Ni_{0.2}Cu_{0.2})Fe_2O_4$	950°C, 10h	1250°C, 10h

TABLE II. High entropy spinels in this study, with firing temperatures and number of hours noted. Sample names correspond with those reported by Musicó *et al.*[35].

of AFe_2O_4 high entropy spinels using magnetometry, neutron powder diffraction, neutron atomic pair distribution function (PDF) studies, and reverse Monte Carlo modeling of spin correlations. We draw several connections between observed magnetic properties, the average and local atomic and magnetic structures, and the influence of material processing history in the series.

II. METHODS

A. Materials Synthesis

In this work, the four phase-pure spinel ferrites originally reported by Musicó *et al.*[35] were synthesized by solid state reaction using identical starting materials and processing conditions. We have elected to use the same naming convention as in the original work, with samples labelled F1, F3, F4, and F5, as noted in TABLE II. Briefly, all the samples were prepared in 5-gram batches using mixtures of stoichiometric proportions of dried precursor oxide powders (MgO, NiO, CoO, CuO, ZnO, MnO_2, and Fe_2O_3). The mixtures were ball milled, pressed into pellets, and heat treated according to the details in TABLE II. Mixtures for samples F1 and F3 were initially heated at 1250°C for 10 hours. Samples F4 and F5 (both containing Mn) were obtained by first heating the mixed powder at 950°C in order to convert the MnO_2 precursor to Mn_3O_4. After the first heating step, all samples were ground, repressed, and sintered a second time at 1250°C for 10 hours. The heat treatment protocols are the same used for the compositions reported in Musicó *et al.*[35], though the heat treatment temperatures and times were not included in the original work.

B. Magnetic Measurement

Magnetometry measurements were performed using a vibrating sample magnetometer (VSM) as part of a Quantum Design PPMS DynaCool system. Temperature-dependent magnetometry (M vs T) was performed using field cooled (FC) and zero field cooling (ZFC) methods. For each sample, a ZFC measurement was first performed by cooling the powder sample to 2 K in the absence of a magnetic field, then applying a 10 mT field and measuring the magnetic moment as the temperature was increased from 2 K to 400 K. After the ZFC measurement, the applied field was kept at 10 mT while measuring the magnetization as the temperature was reduced from 400 K to 2 K for the FC curve. Magnetic hysteresis (M_H) loops between ± 2 T were also measured at temperatures ranging from 2 K and in 25 K steps up to 400 K. All measurements have been normalized to the sample mass.

First order reversal curve (FORC) measurements were performed to evaluate the distribution of magnetic phases and interactions within the samples[73–75]. Following previously published procedures, FORC measurements were performed by first positively saturating the sample, then reducing the magnetic field to a reversal field (H_R). Next, the magnetization is measured as the applied field (H) is increased from H_R back to positive saturation. This sequence was repeated at H_R between the positive and negative saturation. The FORC distribution (ρ) is calculated by applying a mixed second order derivative to the dataset:

$$\rho(H, H_R) = \frac{-1}{2M_S} \frac{\partial^2 M(H, H_R)}{\partial H \partial H_R} \tag{1}$$

where M_S is the saturation magnetization of the sample. FORC measurements were completed at 2 K and 300 K for each sample. While H and H_R separately probe up and down-switching events, respectively, FORC distributions are commonly presented with a change of coordinates from (H, H_R) to:

$$H_C = \frac{H - H_R}{2}, \quad \text{and} \quad H_B = \frac{H + H_R}{2} \tag{2}$$

where H_C and H_B represent the local coercive and bias (interaction) fields, respectively. As all samples show features prominent along axes in both coordinate systems, FORC distributions are presented in (H, H_R) while also indicating the (H_C, H_B) axes. The FORC distributions also include significant reversible components, which are captured using a constant extension mechanism[76].

C. Neutron total scattering

Time of flight (TOF) neutron powder diffraction (NPD) data was collected at 300 K on the Nanoscale Ordered Materials Diffractometer (NOMAD) at the Spallation Neutron Source (SNS) at Oak Ridge National Laboratory (ORNL)[77]. For each sample, approximately 0.3 g of powder was loaded into a 3 mm diameter quartz capillary, placed in a temperature controlled Ar cryostream, and data was collected for 1 h. Data reduction was completed with the Advanced Diffraction Environment (ADDIE) suite[78]. The instrument background and sample container contributions were subtracted, data were corrected for detector deadtime, absorption, and multiple scattering effects, and were normalized by the incident flux and total sample scattering cross section. The maximum value of Q vector used for generation of the PDF was 40 Å^{-1}. The coherent neutron scattering lengths vary considerably among the cations in the sample series, with (in order from smallest to largest) b_{Mn}= -3.73 fm, b_{Co}= 2.49 fm, b_{Cr} = 3.635 fm, b_{Mg}= 5.375 fm, b_{Zn}= 5.68 fm, b_{Cu}=7.718 fm, b_{Fe} = 9.45 fm, and b_{Ni}= 10.3 fm. The neutron scattering length of oxygen is b_O= 5.803 fm.

The experimental diffraction data (31° 2θ detector bank) were analyzed with the Rietveld method as embodied in the TOPAS-V7[79] program. Analysis was completed for each dataset fixing the cation site occupancy according to a normal ($[\text{A}]_{tet}[\text{Fe}_2]_{oct}\text{O}_4$), an inverse ($[\text{Fe}]_{tet}[\text{A,Fe}]_{oct}\text{O}_4$) (Shown in FIG. 1(a)), and a random ($[\text{A}_{1/3}\text{Fe}_{2/3}]_{tet}[\text{A}_{2/3}\text{Fe}_{4/3}]_{oct}\text{O}_4$) spinel structure model ($\text{F}d\bar{3}m$). In all fits, the magnetic scattering was modelled using a magnetic structure model with an $\text{I}4_1/am'd'$ structure featuring one constrained magnetic moment for all tetrahedral sites and one constrained magnetic moment oriented in opposite direction for all octahedral sites (shown in FIG. 1(c)). Background parameters, scale factors, cubic lattice parameters a_{nuc}, isotropic atomic displacement parameters (ADPs) (one for oxygen atoms, one for all cations on the tetrahedral site, and one for all atoms on the octahedral site), instrument profile parameters, and the oxygen atom position (u) were refined for the nuclear structure models. For the refinement of magnetic structure, the isotropic ADPs were constrained to be equivalent to those in the nuclear structure, while the lattice parameters a_{mag}=b_{mag} were constrained to equal $\sqrt{2}a_{nuc}/2$ and the lattice parameter c_{mag} was constrained to equal a_{nuc} (according to geometry, FIG. 1(b)). The scale factor of the magnetic phase was constrained to one half that of the nuclear phase (since $\text{V}_{mag}/\text{V}_{nuc}$=1/2). Magnetic moments were refined along the z direction for the magnetic elements sitting on the respective tetrahedral and octahedral sites (constrained as one unique value per lattice site).

PDF refinements and model simulations were completed using normal, inverse spinel and the random solution models in the PDFgui[80] program, and included a scale factor, lattice parameters, quadratic peak sharpening parameters for correlated atomic motion, and isotropic ADPs. Instrument parameters for real-space dampening and broadening were fixed to values determined through refinement of a silicon crystalline standard reference material.

D. Reverse Monte Carlo Modeling

RMC modeling involving both total scattering and Bragg data was conducted using the RMCProfile package [81]. Fits for both neutron $F(Q)$ and neutron Bragg data were completed. $F(Q)$ is defined by

$$F(Q) = (\sum_{i=1}^{n} c_i \bar{b}_i)^2 \, (S(Q) - 1) \,, \tag{3}$$

where $Q = k - k'$ is the scattering vector of length $4\pi sin\theta/\lambda$ for a neutron of wavelength λ scattered at an angle 2θ, and k and k' are the initial and final wavevectors of the scattered neutron, respectively. $S(Q)$ is the normalized total-scattering structure factor. $\bar{b}_i$ is the coherent bound neutron scattering length of species i, averaged over the different isotopes and nuclear spin states of i. c_i is the portion of species i in the material[82]. A 10×10×10 supercell was first built, based on the unit cell model obtained via Rietveld refinement for each sample. The supercell structural configuration was then optimized in a data-driven manner, following the Metropolis approach. Two sets of RMC modeling was completed for each sample, assuming either inverse or random site occupancy (the normal model was excluded because of the poor agreement demonstrated by Rietveld refinements). No atomic position swapping was allowed between tetrahedral and octahedral sites. In the original report by Musicó et al., multiple valence states for Fe and Mn were detected among high entropy spinels via X-ray absorption spectroscopy. Thus, RMC trials were performed for several samples assuming various valence states for Fe and Mn atoms (since valence determines the magnetic form factors assigned). Here, it should be pointed out that the magnetic moment vectors in RMC configurations are unit vectors with magnetic moment magnitude specified (fixed) according to each cation involved. The bond valence sum (BVS) constraint in RMC fitting is implemented in such a way that it effectively constrains the net valence of the whole system to be 0. The findings discussed in this report were found to be independent of the valence settings in RMCProfile. The final configurations were initiated assuming a +2 valence state for all A cations in the AFe_2O_4 compositional series, and a +3 valence state for the remaining two Fe cations.

Neutron total scattering structure factor data, F(Q), and Bragg data were used for RMC modeling, since the calculation for magnetic diffuse scattering is performed only in Q-space in RMCProfile. For the inclusion of Bragg data in RMC modeling, peak profiles and background were extracted from Topas refinement and tabulated for RMCProfile to read in – hence the RMC engine only calculates peak intensities. In addition to the experimental data, a minimum distance for each single pair of atoms and an overall bond valence sum were added as model constraints. Given multiple constraints exerted upon the structural model, an automatic weight assigning scheme[83] was used.

A kernel density estimation (KDE) and the Henze-Zirkler (HZ) statistic were utilized to interpret variation in the distribution of atom sites and magnetic spin correlations resulting from RMC model fits to neutron total scattering data. KDE is a commonly used method for estimating the underlying probability distribution function in a collection of data points with a non-parameterized approach. Here, the standard normal function is used as the kernel and in practice that means one would have a standard normal distribution function with the center at each of the data points. The overall distribution function is then composed of all those kernels, while being normalized to give the overall distribution probability of 1. The HZ parameter[84–87] is a parameter characterizing the normality of a distribution and the closer its value gets to 1, the closer that underlying distribution is to a Gaussian distribution. The following equation defines the HZ parameter:

$$HZ = [\frac{1}{n}\sum_{i=1}^{n}\sum_{j=1}^{n} e^{-\frac{\beta^2}{2}D_{ij}}] - [2(1+\beta^2)^{-\frac{d}{2}}\sum_{i=1}^{n} e^{-\frac{\beta^2}{2(1+\beta^2)}D_i}] + [n(1+2\beta^2)^{-\frac{d}{2}}], \tag{4}$$

where D_i is the squared Mahalanobis distance of the i^{th} observation to the centroid and D_{ij} gives the squared Mahalanobis distance between i^{th} and j^{th} observations:

$$D_i = (\overrightarrow{x}_i - \overrightarrow{\bar{x}})^T S^{-1} (\overrightarrow{x}_i - \overrightarrow{\bar{x}}), \tag{5}$$

$$D_{ij} = (\overrightarrow{x}_i - \overrightarrow{x}_j)^T S^{-1} (\overrightarrow{x}_i - \overrightarrow{x}_j), \tag{6}$$

β is given by

$$\beta = \frac{1}{\sqrt{2}}(\frac{n(2d+1)}{4})^{\frac{1}{d+4}}, \tag{7}$$

which includes the particle sample size n_p and sample dimensions d.

III. RESULTS AND DISCUSSION

A. Entropy, Energy, and predicted site preference

The cation distribution in high entropy spinels will be impacted by a number of thermodynamic and crystal-chemical factors. The CFSE of the oxygen ligand field and the S_{config} resulting from the number of participating cations are two important factors. The electron configuration energy difference between ligand field and isotropic field is defined as CFSE,

$$CFSE = \Delta E = E_{ligand\,field} - E_{isotropic\,field}. \tag{8}$$

The CFSE can be straightforwardly calculated for each participating cation assuming a specific charge state and either an octahedral or tetrahedral geometry, and the net CFSE can be compared for specific distributions of cations to evaluate potential site preferences.

The CFSE for the four compositions in the AFe_2O_4 series are shown in FIG. 2 (a), assuming a +2 valence state for all five cations on the A site, and a +3 valence state for the remaining two Fe cations. Regardless of the oxidation state used in calculations, the CFSE of the inverse structure model is the lowest among the model spinel structures while the CFSE of the normal structure model is the highest.

The entropy contribution made by the compositional mixture on the tetrahedral and octahedral lattice sites will differ for normal, inverse, and random spinels. The ideal S_{config} per cation for HEOs with multiple cations occupying different sublattice sites can be calculated[68] by

$$\frac{S_{config}}{cation} = -R\frac{\sum_{x=1}^{x} a^x \sum_{N=1}^{N}(f_i^x ln f_i^x)}{cation}, \tag{9}$$

where R is the universal gas constant, a^x is the number of sites on the x sublattice, f_i^x is the fraction of elemental species occupied on the respective sublattice, and N is the number of elements in a given sublattice. For example, for the normal spinel AFe_2O_4, Equation 9 can be evaluated as

$$\frac{S_{config}}{cation} = \frac{S_{config}}{3} = -R\frac{1*(5*0.2ln0.2)+2*1ln1+4*1ln1}{3} \approx 0.54R. \qquad (10)$$

As shown in FIG. 2(b) the random spinel offers the highest entropy contribution, regardless of the number N of cations on the A sublattice site of AFe_2O_4 (from 1 to 8, with Fe not included), followed by the inverse and normal spinel configurations. The S_{config} calculations for N from 1 to 8 with Fe from the B site included are also completed in FIG. S1. Since F3 and F4 do not have Fe on the A site their S_{config}s are larger than those of F1 and F5 when random and inverse spinel models are considered, respectively. It is worth noting that the S_{config}s for the compositions in the series are all smaller than $1.5R$, meaning the spinels do not meet the classic definition of a high entropy oxide (or even medium entropy oxide). In thermodynamic terms, these compositions are more accurately classified as compositionally complex oxides (CCOs).

To summarize, the CFSE and S_{config} terms for AFe_2O_4 spinels provide competing drivers for cation site selectivity, favoring inverse versus random cation configurations, respectively. Observed cation distributions could very well be influenced by the sample-specific processing procedures.

B. Magnetic Measurements

Results of temperature- and field-dependent magnetometry for the samples in our study are shown in FIG. 3 and FIG. 4 (a), respectively. For all of the samples, the black, dashed ZFC curve shows a continuous increase with increasing temperature, indicating the enhanced role of thermal fluctuations by reorienting the magnetization with the magnetic field. Also, the ZFC curve is well separated from the FC curve, with no apparent inflection, and the FC curve is smooth and persistently non-zero, indicating the system does not have a blocking temperature and is not superparamagnetic in this temperature range. This is consistent with the previous work by Musicó et al.[35], which identified the Néel temperature (T_N) of > 400K; the Néel temperature of other spinel ferrites includes 858K for Fe_3O_4 and 725K for $CoFe_2O_4$. These conclusions are also consistent with the M_H loops, shown in FIG. 4 (a), which show that every sample has a very small, but non-zero, coercivity ($\approx$ 2-5 mT) at 300 K.

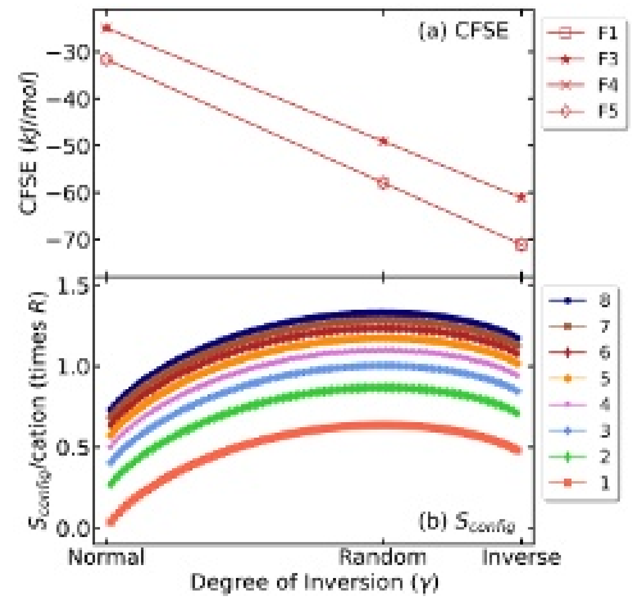

FIG. 2. (a) The CFSE calculations for F1 (□), F3 (★), F4 (×),and F5 (◊) with normal spinel, random solution, and inverse spinel structure models assumed (with a +2 valence state for all A cations in the AFe_2O_4 compositional series, and a +3 valence state for the remaining two Fe cations). (b) The calculated S_{config} of AFe_2O_4 high entropy spinels with the degree of inversion (γ) changing from 0 to 1 and the assumption that there are N (from 1 to 8, Fe is not included) cations occupying the A site (the γ values 0, 2/3, and 1 were labeled according to the corresponding normal, random solution, and inverse spinel structure configurations).

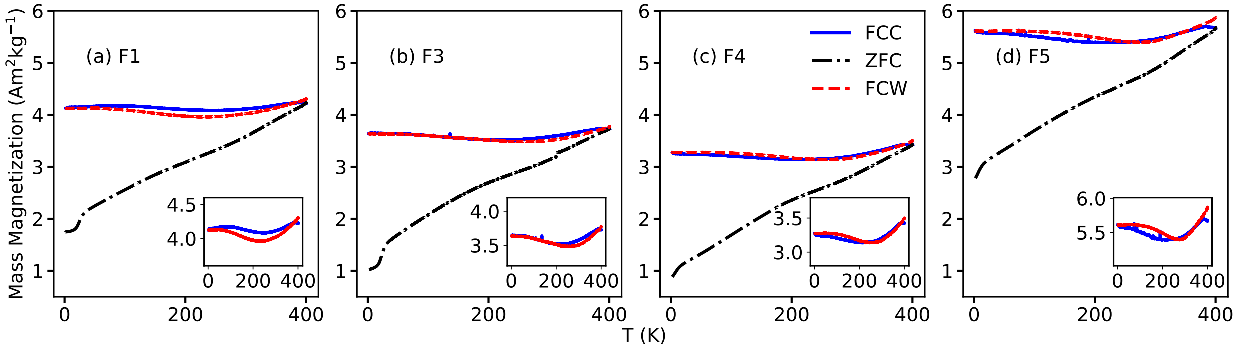

FIG. 3. The comparison of field-cooled (FC), zero-field-cooled (ZFC), and zero-field-warming (FCW) for all ferrite samples measured from 2K to 400K with an applied field of 10 mT: (a) F1, (b) F3, (c) F4, and (d) F5. The legend in (c) applies to all subplots. The insets are displayed in order to emphasize the cross-over and hysteresis in the FC and FCW curves.

The field-dependent magnetometry measurements of F1, F3, F4, and F5 samples in this study are shown in FIG. 4 (a), the measurements completed by Musicó et al.[35] are reproduced in FIG. 4 (b) for comparison. This comparison shows significant differences in the M_H loops, with the samples in this work having a nearly constant (compositionally independent) magnetic saturation (M_S) and an exceedingly small coercivity in all of the samples. By comparison, the samples from Musicó et al.[35] shows a variable M_S between the different samples, with F3 being particularly large, while the others are similar to the current work. Also the coercivity in Ref. [35] is generally larger than the current work, especially F5. The two batches of samples were synthesized in the same laboratory, by the same researcher, using the same batch size, grinding and sintering procedure, and precursors from the same supplier. The only known change in sample preparation involved a replaced heating element for the furnace used. Additionally, the magnetometry measurements of samples prepared for Musicoó et al.[35] were completed soon after synthesis, whereas and mangetometry measurements of samples prepared in the present work was completed two years after synthesis. The observed difference in magnetic behavior among samples of the same composition suggests a potential high sensitivity to synthesis and processing conditions, and/or ageing, in high entropy spinels, and deserves further investigation. For consistency, it is important to note that the M_H loops in this work were field cooled in 10 mT, while Ref. [35] uses 100 mT. This difference would manifest if the system has an antiferromagnetic phase coupled to the ferromagnetic phase or high anisotropy phase with a saturation field larger than the 2 T applied here. In these cases, the hysteresis loop would be vertically and horizontally shifted in FIG. 4 due to the exchange bias effect. The absence of these features suggests that the cooling field is not responsible for the observed differences.

C. Distinct Small Magnetic Clusters

The differences in the M_H plots maybe the result of a strong sensitivity to local compositional distributions and microstructure. This sensitivity would manifest in the magnetic reversal behavior of the sample, which can be probed using the FORC technique. The calculated FORC distributions are shown in FIG. 5 at 2 K (a,c,e,g) and 300 K (b, d, f, h) for all samples.

The FORC distributions all show their primary feature aligned along the H_B axis with

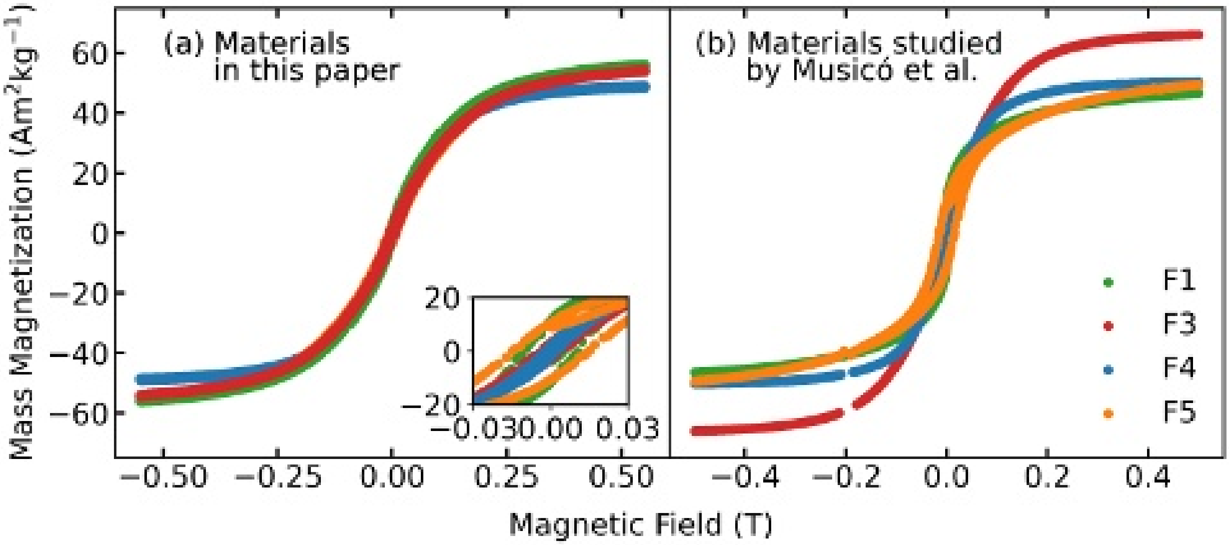

FIG. 4. The comparison of magnetic hysteresis loop data for ferrite compositions (F1,F3,F4,F5) measured at 300K with a ± 0.5 T range for (a) materials in this paper, measured with a 10 mT cooling; and (b) materials studied by Musicó et al., measured with a 100 mT cooling. The legend in (b) applies to both subplots.

a small feature in the H_C direction which is more prominent at low temperatures. A small bump in the H_R direction is also seen at 2 K but is absent at room temperature. While these features are present for all of the samples, they vary in intensity and prominence, with the attributes being lowest for sample F3.

The FORC distribution encodes a map of the switching events within a particular hysteretic system. The bias-field axis identifies the shift from $H = 0$ of a particular set of switching events. For a system without exchange bias, this shift can be attributed to interactions within the sample. The FORC distribution shown here has a wide spread in H_B, indicating strong demagnetizing interactions, e.g. interactions which drive the system away from a saturated configuration[75, 88]. These interactions can be the result of dipolar coupling or exchange-motivated frustration. The presence of long-range ferrimagnetic magnetic ordering without a blocking temperature, and with only a very small coercivity, suggests the interactions are likely due to frustration. At low temperatures, the protrusion along the H_C axis suggests the intrinsic anisotropy has increased compared to the room temperature measurements. The protrusion along the H/H_R axes indicate some of the sample reverses by a domain nucleation/propagation mechanism[89]. The appearance of the domain rever-

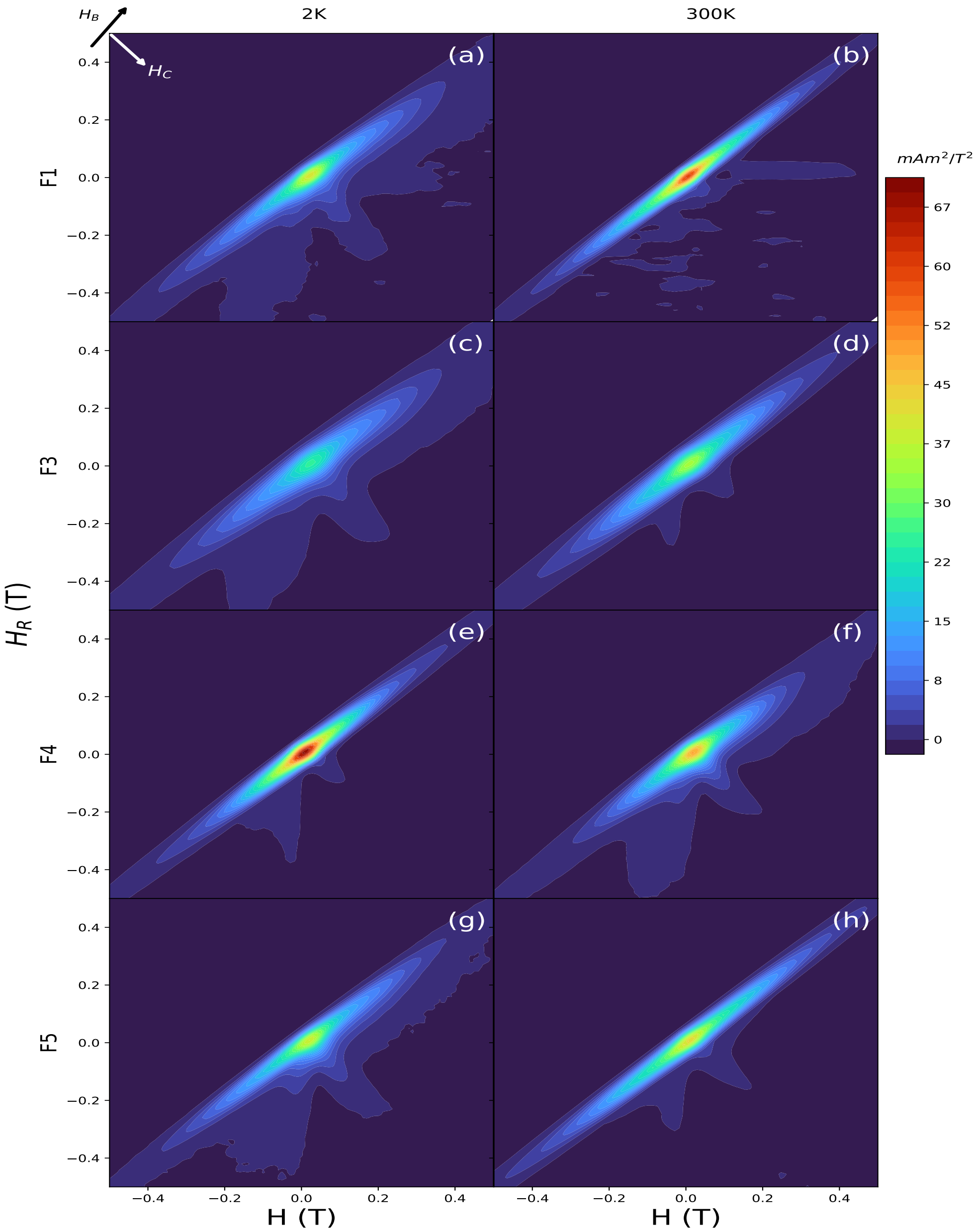

FIG. 5. The comparison of FORC measurements at 2 K and 300 K for sample F1 (a,b), F3 (c.d), F4 (e,f), and F5 (g,h), respectively. The directions of H_B and H_C are plotted for clarification and the scale bar indicates the rate at which the magnetic reversal speed changes for different H_R.

sal mechanism indicates that large areas of the sample have become magnetically coupled and can support domain growth through their boundaries. Complementary to this, the higher temperature samples may consist of magnetic islands, or regions which are coupled by non-magnetic or antiferromagnetic phases.

D. Average Structure

The neutron diffraction patterns of all four samples appear visually similar (FIG. 6 (a)) and can be indexed to a cubic spinel $Fd\bar{3}m$ structure model with corresponding $I4_1/a'd'$ ferrimagnetic ordering model, with no detected secondary phases. Distinguishing cation order is challenging with Bragg diffraction data. The scattering length of involved elements, the degree of cation inversion, and the magnetic order on the cation sublattice may all contribute to observed variation in peak intensities. As a demonstration, the calculated neutron diffraction patterns for nuclear and magnetic scattering assuming inverse, random, and normal spinel structure models with assumed ferrimagnetic spin order for each sample are shown in FIG. S2. It can be seen in FIG. 6(a) that the nuclear Bragg peak intensities are higher for F1 and F3 samples relative to F4 and F5 samples. The intensities of dominant magnetic peaks (for example, the (331) and (111) reflections) appear similar for all compositions.

Separate Rietveld refinements assuming normal, random, and inverse spinel models were completed for each sample (TABLE S1 for F1, TABLE S2 for F3, TABLE S3 for F4, TABLE S4 for F5), each incorporating the ferrimagnetic structure shown in FIG. 1 (c). A summary of Rietveld refinement results is presented in TABLE III. The Rietveld refinement results reveal distinct preference in cation site ordering. For all samples, the normal spinel structure model resulted in poor agreement and nonsensical magnetic moments. The combination of inverse spinel and ferrimagnetic model fits the data better than those of random and normal spinel models for F1 and F3 samples (the F1 result is shown in FIG.6(b)), while the combination of random solution spinel and ferrimagnetic model fits the data better than normal and inverse models for F4 and F5 samples (the F4 result is shown in FIG.6(c)). The ferrimagnetic scattering contributes 100% to the hkl peak (331), a large portion to the peaks (531), (222), (111), and some percentage to the (422), (400), and (220) peaks. The intensity of peaks with combination contributions from nuclear and magnetic structures are not precisely fit with either random or inverse structure; the average structures may lie somewhere in between. Since the nuclear Bragg peaks are overlapped with the magnetic Bragg peaks and there are a high number of participating cations, Bragg diffraction data alone is not enough to determine the detailed structure and cation site preferences of the high entropy spinels.

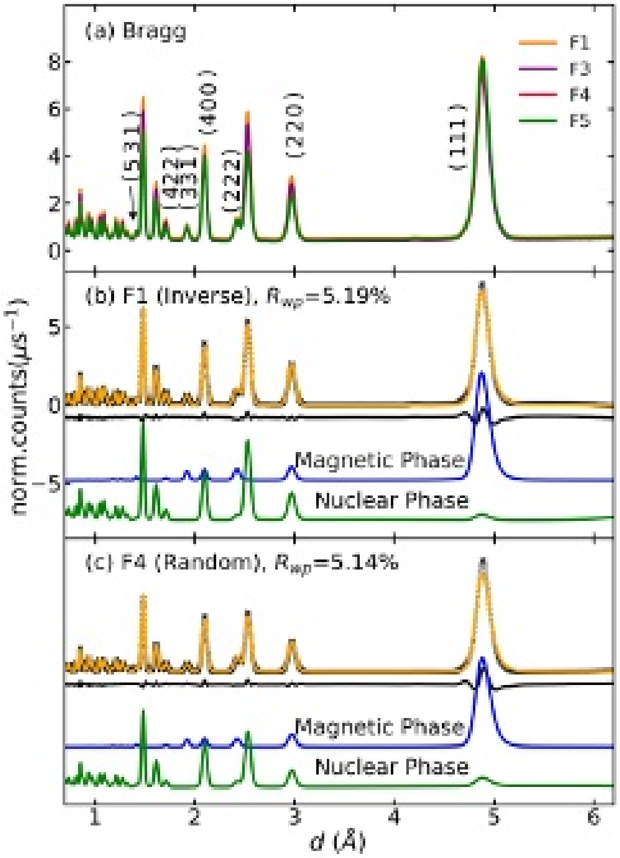

FIG. 6. (a) The comparison of neutron Bragg data (31° detector bank) from F1 (orange line), F3 (purple line), F4 (red line), and F5 (green line) samples. Several hkl peaks featuring ferrimagnetic contributions are labeled. Best-fit Reitveld refinement of (a) F1 data using inverse spinel and ferrimagnetic spin order model and (c) F4 data using random solution spinel and ferrimagnetic spin order model. In (b) and (c) data are shown as black "x"s, fits are shown as solid orange lines, and difference curves fall below the data and fits in black lines. The blue and green solid curves displayed below the refinement results display the magnetic and nuclear contributions to the fits, respectively.

E. Chemical Short Range Order

A comparison of the neutron PDFs for the high entropy spinels is provided in FIG. 7(a), displayed between 1.7 Å and 10 Å. All pair correlations have been numbered and identified by category with a color key to aid discussion. First, it is immediately apparent that the local atomic configurations of the high entropy spinels in the present study are similar; in particular, the location and peak shapes of nearest-neighbour and nex-nearest neighbor

Sample	F1	F3	F4	F5
Best Model	Inverse	Inverse	Random	Random
M(μ_B/Å)	0.406	0.215	1.162	0.532
a (Å)	8.3796(1)	8.3793(1)	8.3894(1)	8.3839(1)
u (frac.)	0.2440(0)	0.2438(0)	0.2433(0)	0.2436(0)
$U_{iso,8b}$ (Å^2)	0.0057(1)	0.0066(1)	0.0054(1)	0.0069(1)
$U_{iso,16c}$ (Å^2)	0.0040(1)	0.0035(1)	0.0047(1)	0.0069(1)
$U_{iso,32e}$ (Å^2)	0.0079(1)	0.0088(1)	0.0085(1)	0.0084(1)
R_{wp}	5.19	5.28	5.14	4.54

TABLE III. Parameters for the best fitting model results among the normal, inverse and random solution F$d\bar{3}m$ spinel models applied for F1, F3, F4, and F5 Rietveld refinements. The table includes the refined magnetic moment (M), lattice parameter (a), oxygen position (u), isotropic atomic displacement parameters (U_{iso}) for the 8b, 16c, and 32e sites, and the resulting refinement goodness-of-fit, R_{wp}.

pair correlations are coincident across the four compositions. This immediately rules out significant local distortion of specific A site cations. Next, there are specific sets of peaks in the data that vary systematically from sample to sample at low r: the peaks highlighted by magenta (peak 1, 5, 9, 12, 15, 17), green (peak 2, 6, 10, 13), red (peak 4), and pink (peak 8) dashed lines representing A-O, A$_{oct}$-A$_{oct}$/O-O, O-O, and A$_{oct}$-A$_{oct}$/A$_{tet}$-A$_{tet}$/A-O correlations, respectively, are matched in amplitude; the peaks highlighted by sky blue (peak 3, 11, 16) and orange (peak 7, 14), representing A$_{oct}$-A$_{tet}$/A$_{tet}$-A$_{tet}$/A-O and A$_{oct}$-A$_{tet}$/A$_{tet}$-O correlations, respectively, differ in amplitude. Inspection reveals that samples F1 and F3 exhibit similar and higher amplitudes of specific correlations relative to samples F4 and F5. PDF data comparisons for every 10Å across the whole range (1.7-50 Å) are shown in FIG. S3.

Neutron PDF refinements in FIG. 7 (b) and (c) show the effect of changing the cation ordering model (inverse, normal, random configuration models) for F1 and F4 samples, respectively. Fits for F3 and F5 are shown in Supporting Information FIG. S4, and provide similar results to F1 and F4, respectively. It is highly likely the unfit residual is in part due to magnetic spin correlations that are unaccounted for in the models[90, 91]. At present there are no PDF data refinement programs that allow for shared site occupancy and magnetic PDF refinement, thus we have elected to present the nuclear structure fits alone here and address magnetic spin correlations separately. The 15^{th} pair amplitude (an A-O correlation at approximately 8.75Å) is shown to be sensitive to the degree of inversion in spinel ferrite models. Overall, for F1 and F3, the random model and inverse model provide a very similar fit quality and cannot be easily distinguished with PDF refinement. For sample F4 and F5, the fit quality for a random model is superior to that for an inverse model. These results correlate well to conclusions drawn from Rietveld refinement. However, no further conclusion can be made from PDF refinement due to the high numbers of cations present per site and the limitation of existing software for exploring local nuclear and magnetic cation ordering together.

F. Large Box Reverse Monte Carlo (RMC) Modeling

As noted above, quantitative real-space refinement of the series of data is complicated by the presence of magnetic spin correlations and the large number of cations involved on the spinel tetrahedral and octahedral sublattices. Large box modeling of PDF data with nuclear and magnetic spin correlations was pursued to provide additional insight into structure-property characteristics in the series. Combined fits of $F(Q)$ (FIG. S5, FIG. S6) and Bragg (FIG. S7, FIG. S8) intensities were completed for all samples assuming an inverse spinel model and a random solution spinel model (trials with a normal spinel model were not tried as they were ruled out conclusively by Rietveld analysis and small box PDF modeling). The agreement of fits to experimental data is high for both model types for all four samples. TABLE S5 (for F1 and F3) and TABLE S6 (for F4 and F5) list the resulting anisotropic atomic displacement parameters (ADPs) on cation tetrahedral sites, cation octahedral sites, and oxygen sites of each RMC refinement for F1, F3, F4 and F5. For F4 and F5 samples, resulting ADP values for the tetrahedral sites and for oxygen positions in the random solution spinel model fits are found to be nearly half those found for inverse spinel model fits. Such an anomaly, combined with Rietveld refinement results, indicate a strong preference for a random model over an inverse one for F4 and F5 samples. Thus the following discussion

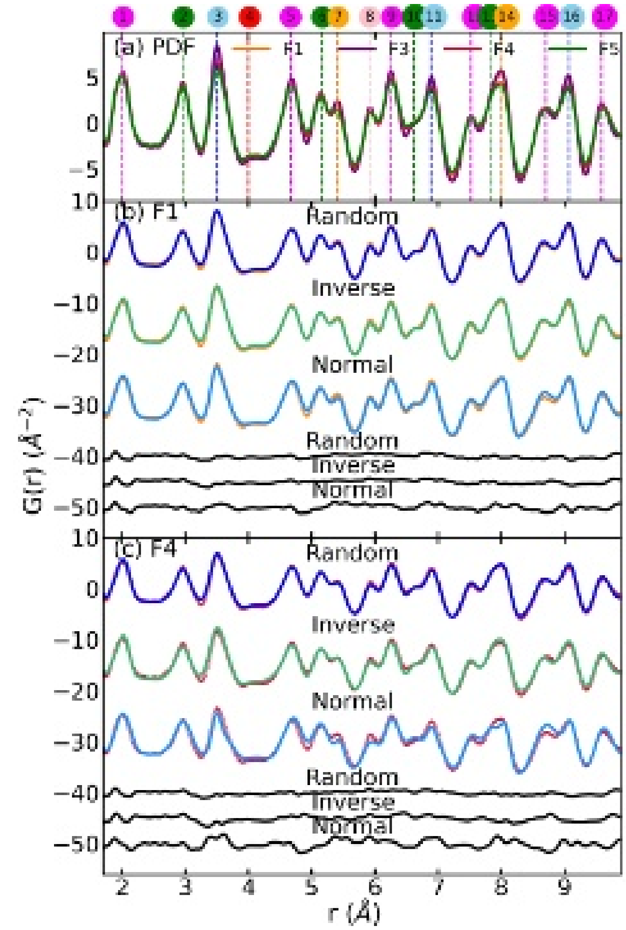

FIG. 7. (a) The PDF data comparison of F1 (orange line), F3 (purple line), F4 (red line), F5 (green line). The 6 peaks (1, 5, 9, 12, 15, 17) highlighted with magenta dashed lines correspond to A-O pairs. The 4 peaks (2, 6, 10, 13) indicated with green dashed lines arise from A_{oct}-A_{oct} and O-O pair correlations. The 3 peaks (3, 11, 16) contributed by A_{oct}-A_{tet},A_{tet}-A_{tet} and A-O are identified in sky blue dashed lines. The peak (4) around 4 Å highlighted in a red dashed line corresponds to an O-O correlation. The combination of A_{oct}-A_{tet} and A_{tet}-O pair correlations contribute the 2 peaks (7, 14) indicated by orange dashed lines. The peak (8) highlighted by a pink dashed line arises from A_{oct}-A_{oct},A_{tet}-A_{tet} and A-O pair correlations). A comparison of the PDF refinements for (b) F1 sample data and (c) F4 sample data using different structure models (random, inverse, and normal spinel ferrite models). PDF data for F1 and F4 samples are shown in orange and red dots, respectively. The blue, lemon green and sky blue solid curves present fits to the data completed with the random solution spinel structure, inverse spinel structure and normal spinel structure model, respectively. The fit difference curves displayed below the data and fits are represented as black solid curves.

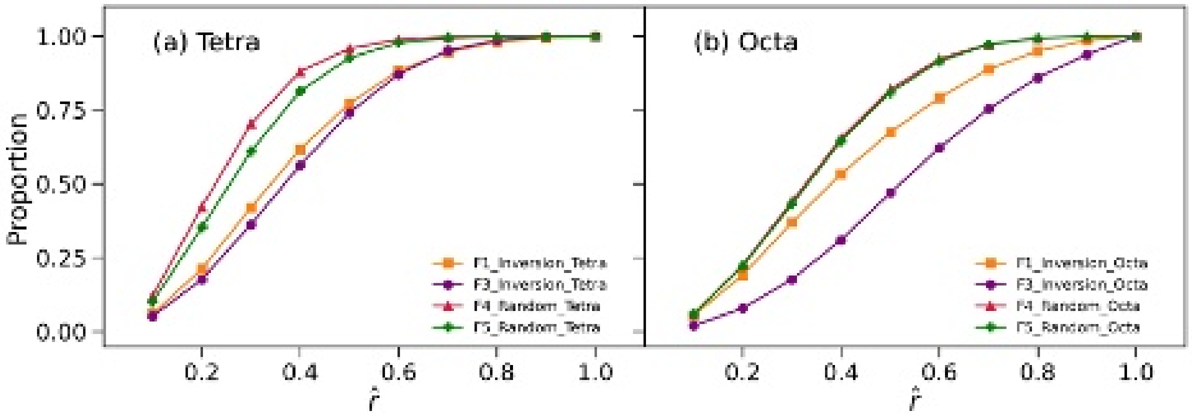

FIG. 8. The proportion of magnetic moment vectors with projection on the XY plane for samples F1, F3, F4 and F5 falling into specified radii, relative to atoms of (a) tetrahedral (Tetra) and (b) octahedral (Octa) sites that the corresponding magnetic moments belong to. Results presented correspond to an inverse spinel structure model for F1 and F3 sample data and a random solution spinel model for F4 and F5 sample data. It is noted that similar results are obtained when the alternate models are used (inverse spinel model for F1 and F3 sample data and random solution spinel model for F4 and F5 samples).

is based on analysis of the model configurations obtained from an inverse spinel model for samples F1 and F3 and a random solution spinel model for samples F4 and F5.

With the magnetic spin configuration obtained via RMC modeling for all samples, all magnetic moment vectors contained in the supercell were mapped into a single unit cell and then projected onto the XY plane. Results are shown visually in Supporting Information FIG. S9 and FIG. S10, the magnetic spin distribution of F1 and F3 samples are more disperse on both tetrahedral and octahedral sites than F4 and F5. In all samples, the magnetic spin distributions of octahedral sites are more disperse than those found on tetrahedral sites. Overall, less collinear spin order and stronger displacements from atom sites are observed for F1 and F3 samples. Two types of statistical analyses were completed to quantify the findings. First, a KDE analysis was conducted, capturing the proportion of magnetic moments found within a specified radius (with the variation ranging from 0 to 1). In principle, the faster such a proportion approaches 1, the stronger the collinearity in magnetic ordering. The results are presented in FIG. 8 (a) for the tetrahedral site magnetic vector distribution and (b) for the octahedral site magnetic vector distribution, indicating a significantly more

PLEASE CITE THIS ARTICLE AS DOI:10.1063/5.0123728

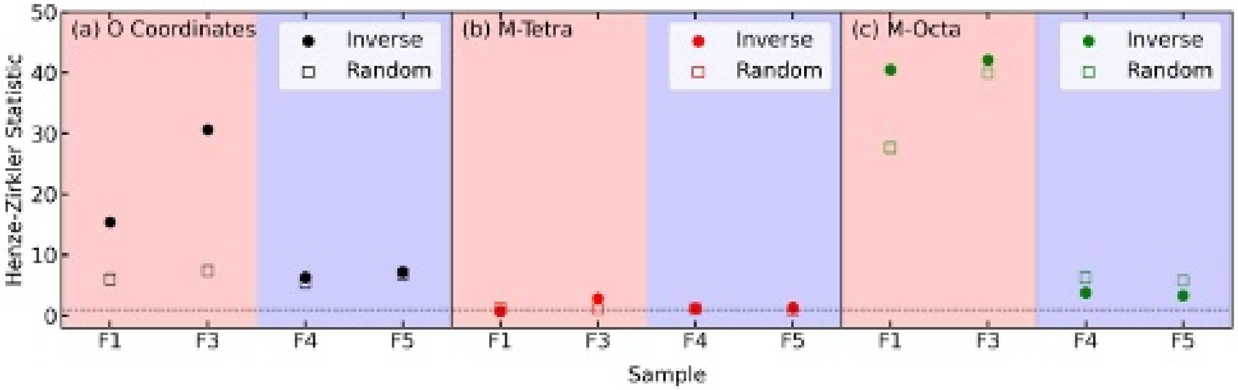

FIG. 9. The HZ statistic for the distribution of (a) oxygen atom (O) coordinates and magnetic moment vectors (M) on (b) tetrahedral sites (Tetra) and (c) octahedral sites (Octa), for F1, F3, F4, and F5 samples. The horizontal dashed lines indicate a Gaussian distribution.

collinear spin arrangement in F4 and F5 samples than in F1 and F3 samples. This result is consistent with the smaller net magnetic moment in F1 and F3 samples - see TABLE S7 in the SI. Additionally, in all samples, tetrahedral site spin correlations are found more collinear than octahedral site spin correlations.

Second, the HZ statistic was calculated to quantify the non-Gaussian behavior of the oxygen coordinate distributions and magnetic moment vectors within the XY plane. Different starting cation distribution configurations are found to influence the HZ statistic values for F1 and F3 samples; however, values determined for F1 and F3 are generally larger than those found for F4 and F5. Overall, in FIG. 9(a) and FIG. 9 (c)., it can be observed that F1 and F3 samples exhibit a more non-Gaussian behavior in oxygen atom distributions and in magnetic moment vector distributions on the octahedral site than F4 and F5 samples. (HZ parameters for F4 and F5 samples are much closer to 1, i.e., no obvious non-Gaussian distortion could be observed). Meanwhile, if focusing on magnetic moment vector distributionson the tetrahedral site (FIG. 9 (b)), all four samples show HZ parameter values close to 1, indicating a nearly Gaussian distribution. These comprehensive results here suggest strong coupling between non-collinear magnetic correllations originating primarily from octahedral site spins and oxygen site displacements, especially in F1 and F3 samples. Variation in the level of spin-lattice coupling among high entropy spinels of similar composition demonstrates a potentially tunable interaction in the more extended family.

IV. CONCLUSION

We have determined the average ferrimagnetic structure in a family of AFe_2O_4 high entropy spinels with neutron Bragg diffraction analysis and found evidence for a variation in the tetrahedral and octahedral site occupancies of A site cations with local structure analysis of neutron total scattering data. These high entropy spinels are not found to have strictly random cation configuration structures (highest S_{config}), but rather, F1/F3 samples in this study were found to have configurations closer to an inverse spinel. The distinct populations of Fe and other magnetic cations on tetrahedral and octahedral sites in the samples manifests in variation in the prevalence and propagation of local spin clusters, as revealed by FORC analysis of magnetometry data. RMC modeling reveals spin non-collinearity in all four samples, enhanced in cases presenting a larger degree of cation inversion.

While identifying the cause for the variation in cation disorder among similar compositions falls outside the scope of the present study, we bring attention to a potential competition between crystal field stabilization effects (which promotes inverse spinel ferrite configurations for the compositions studied) and the entropy stabilization present in truly random spinel ferrite configurations. How much the relative effects of these phenomena are influenced by sample synthesis conditions or other factors, potentially creating samples in one of many different metastable states, remains unknown. Overall, this work highlights that it may prove extremely challenging to achieve a true solid solution with ideal/homogeneous cation mixing in compositionally complex ceramics with complex energy landscapes. We suggest great care be taken in this community to precisely describe reaction conditions, etc. when reporting HEO properties and drawing conclusions regarding the effects of configurational entropy on resultant products. Additionally, experimental characterization of the local to long-range crystal-chemical structure in HEOs may be key to determining and understanding their physical properties. The limitations of the characterization methods explored herein indicate future efforts are needed towards combined experimental probes and advanced data modeling. Hard and soft X-ray absorption near edge spectroscopy (XANES), soft X-ray magnetic circular dichroism (XMCD) and ^{57}Fe Mössbaruer spectroscopy (with and without external magnetic field) are examples of techniques that may provide additional insights.

V. SUMMPLEMENTARY MATERIAL

See supplementary material for additional configurational entropy calculations, average structure results from Rietveld refinement, and local structure results from small-box PDF refinement and large box RMC modeling.

VI. ACKNOWLEDGEMENT

KP acknowledges financial support from the National Science Foundation (DMR-2145174). This research used beamline 1B (NOMAD) of the Spallation Neutron Source, a DOE Office of Science User Facility operated by the Oak Ridge National Laboratory. We acknowledge Dr. Jue Liu for helpful discussion regarding Rietveld refinements and Namila Liyanage, Nan Tang and Tianyu Li for helpful discussion regarding magnetometry results. DAG and CK were supported by the US Department of Energy (DE-SC0021344).

References

[1] S. Jiang, T. Hu, J. Gild, N. Zhou, J. Nie, M. Qin, T. Harrington, K. Vecchio, and J. Luo, A new class of high-entropy perovskite oxides, Scripta Materialia **142**, 116 (2018).

[2] R. Witte, A. Sarkar, R. Kruk, B. Eggert, R. A. Brand, H. Wende, and H. Hahn, High-entropy oxides: An emerging prospect for magnetic rare-earth transition metal perovskites, Physical Review Materials **3**, 034406 (2019).

[3] R. Witte, A. Sarkar, L. Velasco, R. Kruk, R. A. Brand, B. Eggert, K. Ollefs, E. Weschke, H. Wende, and H. Hahn, Magnetic properties of rare-earth and transition metal based perovskite type high entropy oxides, Journal of Applied Physics **127**, 185109 (2020).

[4] D. A. Vinnik, E. A. Trofimov, V. E. Zhivulin, S. A. Gudkova, O. V. Zaitseva, D. A. Zherebtsov, A. Y. Starikov, D. P. Sherstyuk, A. A. Amirov, A. V. Kalgin, *et al.*, High entropy oxide phases with perovskite structure, Nanomaterials **10**, 268 (2020).

[5] Z. Teng, L. Zhu, Y. Tan, S. Zeng, Y. Xia, Y. Wang, and H. Zhang, Synthesis and structures of high-entropy pyrochlore oxides, Journal of the European Ceramic Society **40**, 1639 (2020).

[6] A. Sarkar, Q. Wang, A. Schiele, M. R. Chellali, S. S. Bhattacharya, D. Wang, T. Brezesin-

ski, H. Hahn, L. Velasco, and B. Breitung, High-entropy oxides: fundamental aspects and electrochemical properties, Advanced Materials **31**, 1806236 (2019).

[7] H. Li, Y. Zhou, Z. Liang, H. Ning, X. Fu, Z. Xu, T. Qiu, W. Xu, R. Yao, and J. Peng, High-entropy oxides: Advanced research on electrical properties, Coatings **11**, 628 (2021).

[8] R.-Z. Zhang and M. J. Reece, Review of high entropy ceramics: design, synthesis, structure and properties, Journal of Materials Chemistry A **7**, 22148 (2019).

[9] J. Liu, G. Shao, D. Liu, K. Chen, K. Wang, B. Ma, K. Ren, and Y. Wang, Design and synthesis of chemically complex ceramics from the perspective of entropy, Materials Today Advances , 100114 (2020).

[10] B. L. Musicó, D. Gilbert, T. Z. Ward, K. Page, E. George, J. Yan, D. Mandrus, and V. Keppens, The emergent field of high entropy oxides: Design, prospects, challenges, and opportunities for tailoring material properties, APL Materials **8**, 040912 (2020).

[11] C. Oses, C. Toher, and S. Curtarolo, High-entropy ceramics, Nature Reviews Materials **5**, 295 (2020).

[12] S. H. Albedwawi, A. AlJaberi, G. N. Haidemenopoulos, and K. Polychronopoulou, High entropy oxides-exploring a paradigm of promising catalysts: A review, Materials & Design , 109534 (2021).

[13] Y. Sun and S. Dai, High-entropy materials for catalysis: A new frontier, Science Advances **7**, eabg1600 (2021).

[14] H. Xiang, Y. Xing, F.-z. Dai, H. Wang, L. Su, L. Miao, G. Zhang, Y. Wang, X. Qi, L. Yao, *et al.*, High-entropy ceramics: Present status, challenges, and a look forward, Journal of Advanced Ceramics , 1 (2021).

[15] A. Salian and S. Mandal, Entropy stabilized multicomponent oxides with diverse functionality–a review, Critical Reviews in Solid State and Materials Sciences , 1 (2021).

[16] A. Sarkar, B. Breitung, and H. Hahn, High entropy oxides: the role of entropy, enthalpy and synergy, Scripta Materialia **187**, 43 (2020).

[17] M. Fu, X. Ma, K. Zhao, X. Li, and D. Su, High-entropy materials for energy-related applications, Iscience , 102177 (2021).

[18] S. J. McCormack and A. Navrotsky, Thermodynamics of high entropy oxides, Acta Materialia **202**, 1 (2021).

[19] C. M. Rost, E. Sachet, T. Borman, A. Moballegh, E. C. Dickey, D. Hou, J. L. Jones, S. Cur-

tarolo, and J.-P. Maria, Entropy-stabilized oxides, Nature communications **6**, 1 (2015).

[20] A. Sarkar, R. Kruk, and H. Hahn, Magnetic properties of high entropy oxides, Dalton Transactions **50**, 1973 (2021).

[21] A. Navrotsky and O. Kleppa, Thermodynamics of formation of simple spinels, Journal of Inorganic and Nuclear Chemistry **30**, 479 (1968).

[22] A. Navrotsky and O. Kleppa, The thermodynamics of cation distributions in simple spinels, Journal of Inorganic and nuclear Chemistry **29**, 2701 (1967).

[23] E. Verwey and E. Heilmann, Physical properties and cation arrangement of oxides with spinel structures i. cation arrangement in spinels, The Journal of Chemical Physics **15**, 174 (1947).

[24] E. Gorter, Magnetization in ferrites: saturation magnetization of ferrites with spinel structure, Nature **165**, 798 (1950).

[25] A. El Maazouzi, R. Masrour, and A. Jabar, Thickness-dependent magnetic properties of inverse spinel fe3o4, Phase Transitions **93**, 733 (2020).

[26] R. Anu, K. Vinod, *et al.*, Study of magnetic and optical transitions in MFe_2O_4 (M=Co,Zn,Fe,Mn) with spinel structure, Nanosystems: physics, chemistry, mathematics **12**, 481 (2021).

[27] K. Bouferrache, Z. Charifi, H. Baaziz, A. Alsaad, and A. Telfah, Electronic structure, magnetic and optic properties of spinel compound $NiFe_2O_4$, Semiconductor Science and Technology **35**, 095013 (2020).

[28] S. Selima, M. Khairy, and M. Mousa, Comparative studies on the impact of synthesis methods on structural, optical, magnetic and catalytic properties of $CuFe_2O_4$, Ceramics International **45**, 6535 (2019).

[29] A. Blößer, H. Kurz, J. Timm, F. Wittkamp, C. Simon, S. Hayama, B. Weber, U.-P. Apfel, and R. Marschall, Tailoring the size, inversion parameter, and absorption of phase-pure magnetic $MgFe_2O_4$ nanoparticles for photocatalytic degradations, ACS Applied Nano Materials **3**, 11587 (2020).

[30] F. Sharifianjazi, M. Moradi, N. Parvin, A. Nemati, A. J. Rad, N. Sheysi, A. Abouchenari, A. Mohammadi, S. Karbasi, Z. Ahmadi, *et al.*, Magnetic $CoFe_2O_4$ nanoparticles doped with metal ions: a review, Ceramics International **46**, 18391 (2020).

[31] J. Venturini, A. M. Tonelli, T. B. Wermuth, R. Y. S. Zampiva, S. Arcaro, A. D. C. Viegas, and C. P. Bergmann, Excess of cations in the sol-gel synthesis of cobalt ferrite ($CoFe_2O_4$):

A pathway to switching the inversion degree of spinels, Journal of Magnetism and Magnetic Materials **482**, 1 (2019).

[32] M. Sugimoto, The past, present, and future of ferrites, Journal of the American Ceramic Society **82**, 269 (1999).

[33] C.-W. Nan, M. Bichurin, S. Dong, D. Viehland, and G. Srinivasan, Multiferroic magnetoelectric composites: Historical perspective, status, and future directions, Journal of applied physics **103**, 1 (2008).

[34] J. Dąbrowa, M. Stygar, A. Mikuła, A. Knapik, K. Mroczka, W. Tejchman, M. Danielewski, and M. Martin, Synthesis and microstructure of the $(Co,Cr,Fe,Mn,Ni)_3O_4$ high entropy oxide characterized by spinel structure, Materials Letters **216**, 32 (2018).

[35] B. Musicó, Q. Wright, T. Z. Ward, A. Grutter, E. Arenholz, D. Gilbert, D. Mandrus, and V. Keppens, Tunable magnetic ordering through cation selection in entropic spinel oxides, Physical Review Materials **3**, 104416 (2019).

[36] Z. Grzesik, G. Smoła, M. Miszczak, M. Stygar, J. Dąbrowa, M. Zajusz, K. Świerczek, and M. Danielewski, Defect structure and transport properties of $(Co,Cr,Fe,Mn,Ni)_3O_4$ spinel-structured high entropy oxide, Journal of the European Ceramic Society **40**, 835 (2020).

[37] D. Wang, S. Jiang, C. Duan, J. Mao, Y. Dong, K. Dong, Z. Wang, S. Luo, Y. Liu, and X. Qi, Spinel-structured high entropy oxide $(FeCoNiCrMn)_3O_4$ as anode towards superior lithium storage performance, Journal of Alloys and Compounds **844**, 156158 (2020).

[38] J. Cieslak, M. Reissner, K. Berent, J. Dabrowa, M. Stygar, M. Mozdzierz, and M. Zajusz, Magnetic properties and ionic distribution in high entropy spinels studied by mössbauer and ab initio methods, Acta Materialia **206**, 116600 (2021).

[39] C.-C. Lin, C.-W. Chang, C.-C. Kaun, and Y.-H. Su, Stepwise evolution of photocatalytic spinel-structured $(Co,Cr,Fe,Mn,Ni)_3O_4$ high entropy oxides from first-principles calculations to machine learning, Crystals **11**, 1035 (2021).

[40] S. Marik, D. Singh, B. Gonano, F. Veillon, D. Pelloquin, and Y. Breard, Enhanced magnetic frustration in a new high entropy diamond lattice spinel oxide, Scripta Materialia **186**, 366 (2020).

[41] S. Marik, D. Singh, B. Gonano, F. Veillon, D. Pelloquin, and Y. Bréard, Long range magnetic ordering and magneto-(di) electric effect in a new class of high entropy spinel oxide, Scripta Materialia **183**, 107 (2020).

[42] M. Stygar, J. Dąbrowa, M. Moździerz, M. Zajusz, W. Skubida, K. Mroczka, K. Berent, K. Świerczek, and M. Danielewski, Formation and properties of high entropy oxides in co-cr-fe-mg-mn-ni-o system: Novel (Cr,Fe,Mg,Mn,Ni)$_3$O$_4$ and (Co,Cr,Fe,Mg,Mn)$_3$O$_4$ high entropy spinels, Journal of the European Ceramic Society **40**, 1644 (2020).

[43] M. Fracchia, M. Manzoli, U. Anselmi-Tamburini, and P. Ghigna, A new eight-cation inverse high entropy spinel with large configurational entropy in both tetrahedral and octahedral sites: Synthesis and cation distribution by x-ray absorption spectroscopy, Scripta Materialia **188**, 26 (2020).

[44] B. Liang, Y. Ai, Y. Wang, C. Liu, S. Ouyang, and M. Liu, Spinel-type (FeCoCrMnZn)$_3$O$_4$ high-entropy oxide: facile preparation and supercapacitor performance, Materials **13**, 5798 (2020).

[45] D. Vinnik, E. A. Trofimov, and V. E. Zhivulin, The conditions and results of ferrite based on multicomponent crystal formation in high entropic oxide systems, in *Solid State Phenomena*, Vol. 299 (Trans Tech Publ, 2020) pp. 246–251.

[46] Y. Zhang, T. Lu, Y. Ye, W. Dai, Y. Zhu, and Y. Pan, Stabilizing oxygen vacancy in entropy-engineered CoFe$_2$O$_4$-type catalysts for co-prosperity of efficiency and stability in an oxygen evolution reaction, ACS Applied Materials & Interfaces **12**, 32548 (2020).

[47] T.-Y. Chen, S.-Y. Wang, C.-H. Kuo, S.-C. Huang, M.-H. Lin, C.-H. Li, H.-Y. T. Chen, C.-C. Wang, Y.-F. Liao, C.-C. Lin, *et al.*, In operando synchrotron x-ray studies of a novel spinel (Ni$_{0.2}$Co$_{0.2}$Mn$_{0.2}$Fe$_{0.2}$Ti$_{0.2}$)$_3$O$_4$ high-entropy oxide for energy storage applications, Journal of Materials Chemistry A **8**, 21756 (2020).

[48] H. Chen, N. Qiu, B. Wu, Z. Yang, S. Sun, and Y. Wang, A new spinel high-entropy oxide (Mg$_{0.2}$Ti$_{0.2}$Zn$_{0.2}$Cu$_{0.2}$Fe$_{0.2}$)$_3$O$_4$ with fast reaction kinetics and excellent stability as an anode material for lithium ion batteries, RSC Advances **10**, 9736 (2020).

[49] J. Ma, B. Zhao, H. Xiang, F.-Z. Dai, Y. Liu, R. Zhang, and Y. Zhou, High-entropy spinel ferrites MFe$_2$O$_4$ (M=Mg,Mn,Fe,Co,Ni,Cu,Zn) with tunable electromagnetic properties and strong microwave absorption, Journal of Advanced Ceramics **11**, 754 (2022).

[50] A. Radoń, Ł. Hawełek, D. Łukowiec, J. Kubacki, and P. Włodarczyk, Dielectric and electromagnetic interference shielding properties of high entropy (Zn,Fe,Ni,Mg,Cd)Fe$_2$O$_4$ ferrite, Scientific Reports **9**, 1 (2019).

[51] S. Shaw, A. Gangwar, A. Sharma, S. Alla, S. Kavita, M. Vasundhara, S. S. Meena, P. Maiti,

and N. Prasad, Structural and magnetic properties of nanocrystalline equi-atomic spinel high-entropy oxide $(AlCoFeMnNi)_3O_4$ synthesised by microwave assisted co-precipitation technique, Journal of Alloys and Compounds **878**, 160269 (2021).

[52] A. Mao, F. Quan, H.-Z. Xiang, Z.-G. Zhang, K. Kuramoto, and A.-L. Xia, Facile synthesis and ferrimagnetic property of spinel $(CoCrFeMnNi)_3O_4$ high-entropy oxide nanocrystalline powder, Journal of Molecular Structure **1194**, 11 (2019).

[53] S. Dai, M. Li, X. Wang, H. Zhu, Y. Zhao, and Z. Wu, Fabrication and magnetic property of novel $(Co,Zn,Fe,Mn,Ni)_3O_4$ high-entropy spinel oxide, Journal of Magnetism and Magnetic Materials **536**, 168123 (2021).

[54] A. Mao, H.-Z. Xiang, Z.-G. Zhang, K. Kuramoto, H. Zhang, and Y. Jia, A new class of spinel high-entropy oxides with controllable magnetic properties, Journal of Magnetism and Magnetic Materials **497**, 165884 (2020).

[55] A. Mao, H.-X. Xie, H.-Z. Xiang, Z.-G. Zhang, H. Zhang, and S. Ran, A novel six-component spinel-structure high-entropy oxide with ferrimagnetic property, Journal of Magnetism and Magnetic Materials **503**, 166594 (2020).

[56] H.-Z. Xiang, H.-X. Xie, A. Mao, Y.-G. Jia, and T.-Z. Si, Facile preparation of single phase high-entropy oxide nanocrystalline powders by solution combustion synthesis, International Journal of Materials Research **111**, 246 (2020).

[57] H. Zhu, H. Xie, Y. Zhao, S. Dai, M. Li, and X. Wang, Structure and magnetic properties of a class of spinel high-entropy oxides, Journal of Magnetism and Magnetic Materials **535**, 168063 (2021).

[58] F. H. Mohammadabadi, S. Masoudpanah, S. Alamolhoda, and H. Koohdar, Electromagnetic microwave absorption properties of high entropy spinel ferrite $((MnNiCuZn)_{1-x}Co_xFe_2O_4)$/graphene nanocomposites, Journal of Materials Research and Technology **14**, 1099 (2021).

[59] H.-Z. Xiang, H.-X. Xie, Y.-X. Chen, H. Zhang, A. Mao, and C.-H. Zheng, Porous spinel-type $(Al_{0.2}CoCrFeMnNi)_{0.58}O_{4-\delta}$ high-entropy oxide as a novel high-performance anode material for lithium-ion batteries, Journal of Materials Science **56**, 8127 (2021).

[60] T. Parida, A. Karati, K. Guruvidyathri, B. Murty, and G. Markandeyulu, Novel rare-earth and transition metal-based entropy stabilized oxides with spinel structure, Scripta Materialia **178**, 513 (2020).

[61] G. Wang, J. Qin, Y. Feng, B. Feng, S. Yang, Z. Wang, Y. Zhao, and J. Wei, Sol–gel synthesis of spherical mesoporous high-entropy oxides, ACS Applied Materials & Interfaces **12**, 45155 (2020).

[62] D. Wang, Z. Liu, S. Du, Y. Zhang, H. Li, Z. Xiao, W. Chen, R. Chen, Y. Wang, Y. Zou, *et al.*, Low-temperature synthesis of small-sized high-entropy oxides for water oxidation, Journal of Materials Chemistry A **7**, 24211 (2019).

[63] N. J. Usharani, H. Sanghavi, and S. Bhattacharya, Factors influencing phase formation and band gap studies of a novel multicomponent high entropy $(Co,Cu,Mg,Ni,Zn)_2TiO_4$ orthotitanate spinel, Journal of Alloys and Compounds **888**, 161390 (2021).

[64] A. H. Phakatkar, M. T. Saray, M. G. Rasul, L. V. Sorokina, T. G. Ritter, T. Shokuhfar, and R. Shahbazian-Yassar, Ultrafast synthesis of high entropy oxide nanoparticles by flame spray pyrolysis, Langmuir **37**, 9059 (2021).

[65] T. X. Nguyen, J. Patra, J.-K. Chang, and J.-M. Ting, High entropy spinel oxide nanoparticles for superior lithiation–delithiation performance, Journal of Materials Chemistry A **8**, 18963 (2020).

[66] T. Hirakawa, Y. Shimokawa, W. Tokuzumi, T. Sato, M. Tsushida, H. Yoshida, S. Hinokuma, J. Ohyama, and M. Machida, Multicomponent spinel oxide solid solutions: a possible alternative to platinum group metal three-way catalysts, ACS Catalysis **9**, 11763 (2019).

[67] L. Danyang, S. Liping, L. Qiang, X. Tian, H. Lihua, and Z. Hui, High-entropy oxide $(Fe_{0.2}Zn_{0.2}Co_{0.2}Ni_{0.2}Cu_{0.2})Fe_2O_4$: an efficient and stable spinel-type electrocatalyst for H_2O_2 production in alkaline media, Journal of Alloys and Compounds , 165148 (2022).

[68] A. Sarkar, B. Eggert, R. Witte, J. Lill, L. Velasco, Q. Wang, J. Sonar, K. Ollefs, S. S. Bhattacharya, R. A. Brand, *et al.*, Comprehensive investigation of crystallographic, spin-electronic and magnetic structure of $(Co_{0.2}Cr_{0.2}Fe_{0.2}Mn_{0.2}Ni_{0.2})_3O_4$: Unraveling the suppression of configuration entropy in high entropy oxides, Acta Materialia , 117581 (2021).

[69] E. W. Gorter, Magnetization in ferrites: Saturation magnetization of ferrites with spinel structure, Nature **165**, 798 (1950).

[70] K. R. Sanchez-Lievanos, J. L. Stair, and K. E. Knowles, Cation distribution in spinel ferrite nanocrystals: Characterization, impact on their physical properties, and opportunities for synthetic control, Inorganic Chemistry **60**, 4291 (2021), pMID: 33734686, https://doi.org/10.1021/acs.inorgchem.1c00040.

[71] L. Cervera-Gabalda, A. Zielińska-Jurek, and C. Gómez-Polo, Tuning the photocatalytic performance through magnetization in Co−Zn ferrite nanoparticles, Journal of Magnetism and Magnetic Materials , 169617 (2022).

[72] G. C. Lavorato, R. Das, Y. Xing, J. Robles, F. J. Litterst, E. Baggio-Saitovitch, M.-H. Phan, and H. Srikanth, Origin and shell-driven optimization of the heating power in core/shell bimagnetic nanoparticles, ACS Applied Nano Materials **3**, 1755 (2020), https://doi.org/10.1021/acsanm.9b02449.

[73] C. R. Pike, A. P. Roberts, and K. L. Verosub, Characterizing interactions in fine magnetic particle systems using first order reversal curves, Journal of Applied Physics **85**, 6660 (1999).

[74] A. P. Roberts, C. R. Pike, and K. L. Verosub, First-order reversal curve diagrams: A new tool for characterizing the magnetic properties of natural samples, Journal of Geophysical Research: Solid Earth **105**, 28461 (2000).

[75] D. A. Gilbert, G. T. Zimanyi, R. K. Dumas, M. Winklhofer, A. Gomez, N. Eibagi, J. Vicent, and K. Liu, Quantitative decoding of interactions in tunable nanomagnet arrays using first order reversal curves, Scientific Reports **4**, 1 (2014).

[76] D. A. Gilbert, P. D. Murray, J. De Rojas, R. K. Dumas, J. E. Davies, and K. Liu, Reconstructing phase-resolved hysteresis loops from first-order reversal curves, Scientific Reports **11**, 1 (2021).

[77] J. Neuefeind, M. Feygenson, J. Carruth, R. Hoffmann, and K. K. Chipley, The nanoscale ordered materials diffractometer nomad at the spallation neutron source SNS, Nuclear Instruments and Methods in Physics Research Section B: Beam Interactions with Materials and Atoms **287**, 68 (2012).

[78] M. McDonnell, D. Olds, K. Page, J. Neufeind, M. Tucker, J. Bilheux, W. Zhou, and P. Peterson, Addie: Advanced diffraction environment–a software environment for analyzing neutron diffraction data, Acta Crystallogr., Sect. A: Found. Adv. **73**, a377 (2017).

[79] A. A. Coelho, Topas and topas-academic: an optimization program integrating computer algebra and crystallographic objects written in C++, Journal of Applied Crystallography **51**, 210 (2018).

[80] C. Farrow, P. Juhas, J. Liu, D. Bryndin, E. Božin, J. Bloch, T. Proffen, and S. Billinge, PDFfit2 and PDFgui: computer programs for studying nanostructure in crystals, Journal of Physics: Condensed Matter **19**, 335219 (2007).

[81] M. G. Tucker, D. A. Keen, M. T. Dove, A. L. Goodwin, and Q. Hui, RMCProfile: reverse monte carlo for polycrystalline materials, Journal of Physics: Condensed Matter **19**, 335218 (2007).

[82] D. A. Keen, A comparison of various commonly used correlation functions for describing total scattering, J. Appl. Crystallogr. **34**, 172 (2001).

[83] Y. Zhang, M. Eremenko, V. Krayzman, M. G. Tucker, and I. Levin, New capabilities for enhancement of *RMCProfile*: instrumental profiles with arbitrary peak shapes for structural refinements using the reverse Monte Carlo method, Journal of Applied Crystallography **53**, 1509 (2020).

[84] N. Henze and B. Zirkler, A class of invariant consistent tests for multivariate normality, Communications in statistics-Theory and Methods **19**, 3595 (1990).

[85] S. Flegel, M. Möckel, and J. Bennett, Covariance size and the breakdown of gaussianity in geo uncertainty predictions, in *Proceedings of the 7th European Space Debris Conference* (2017).

[86] S. K. Flegel and J. C. Bennett, State Uncertainty Normality Detection, J. Astronaut. Sci. **67**, 1044 (2020).

[87] A. Trujillo-Ortiz, R. Hernandez-Walls, K. Barba-Rojo, and L. Cupul-Magana, Hzmvntest: Henze-zirkler's multivariate normality test, A MATLAB file , 81 (2007).

[88] C. Pike, C. Ross, R. Scalettar, and G. Zimanyi, First-order reversal curve diagram analysis of a perpendicular nickel nanopillar array, Physical Review B **71**, 134407 (2005).

[89] J. E. Davies, O. Hellwig, E. E. Fullerton, G. Denbeaux, J. Kortright, and K. Liu, Magnetization reversal of Co/Pt multilayers: Microscopic origin of high-field magnetic irreversibility, Physical Review B **70**, 224434 (2004).

[90] B. Frandsen, X. Yang, and S. J. Billinge, Magnetic pair distribution function analysis of local magnetic correlations, Acta Crystallographica Section A: Foundations and Advances **70**, 3 (2014).

[91] B. A. Frandsen and S. J. Billinge, Magnetic structure determination from the magnetic pair distribution function (mPDF): ground state of mno, Acta Crystallographica Section A: Foundations and Advances **71**, 325 (2015).

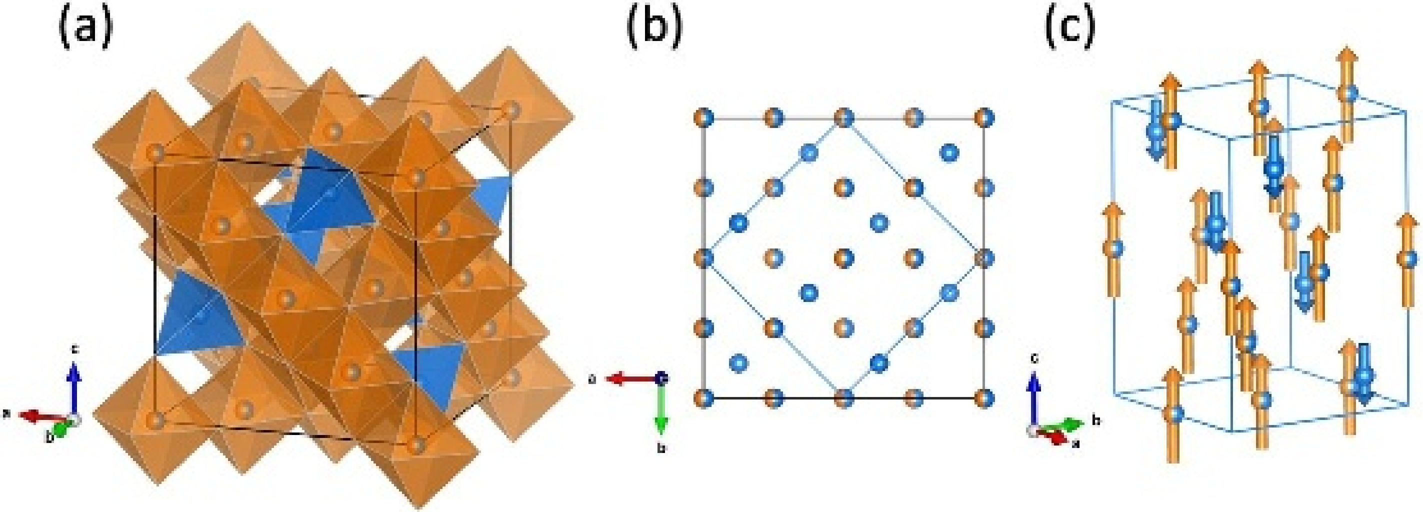
(a)
c
a
b
(b)
a
b
(c)
c
b
a

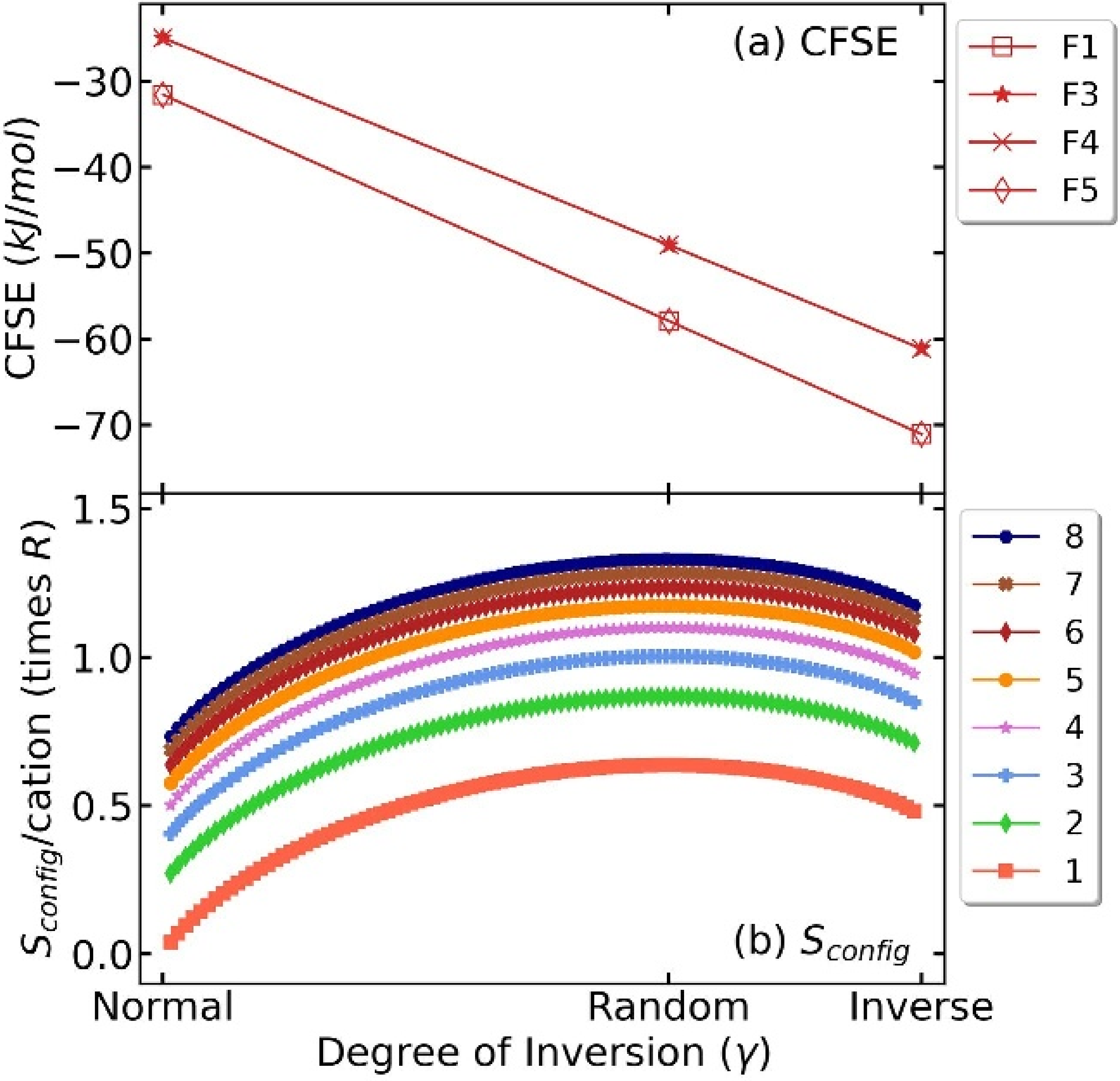
(a) CFSE
CFSE (kJ/mol)
−30
−40
−50
−60
−70
F1
F3
F4
F5
(b) S_{config}
S_{config}/cation (times R)
1.5
1.0
0.5
0.0
8
7
6
5
4
3
2
1
Normal
Random
Inverse
Degree of Inversion (γ)

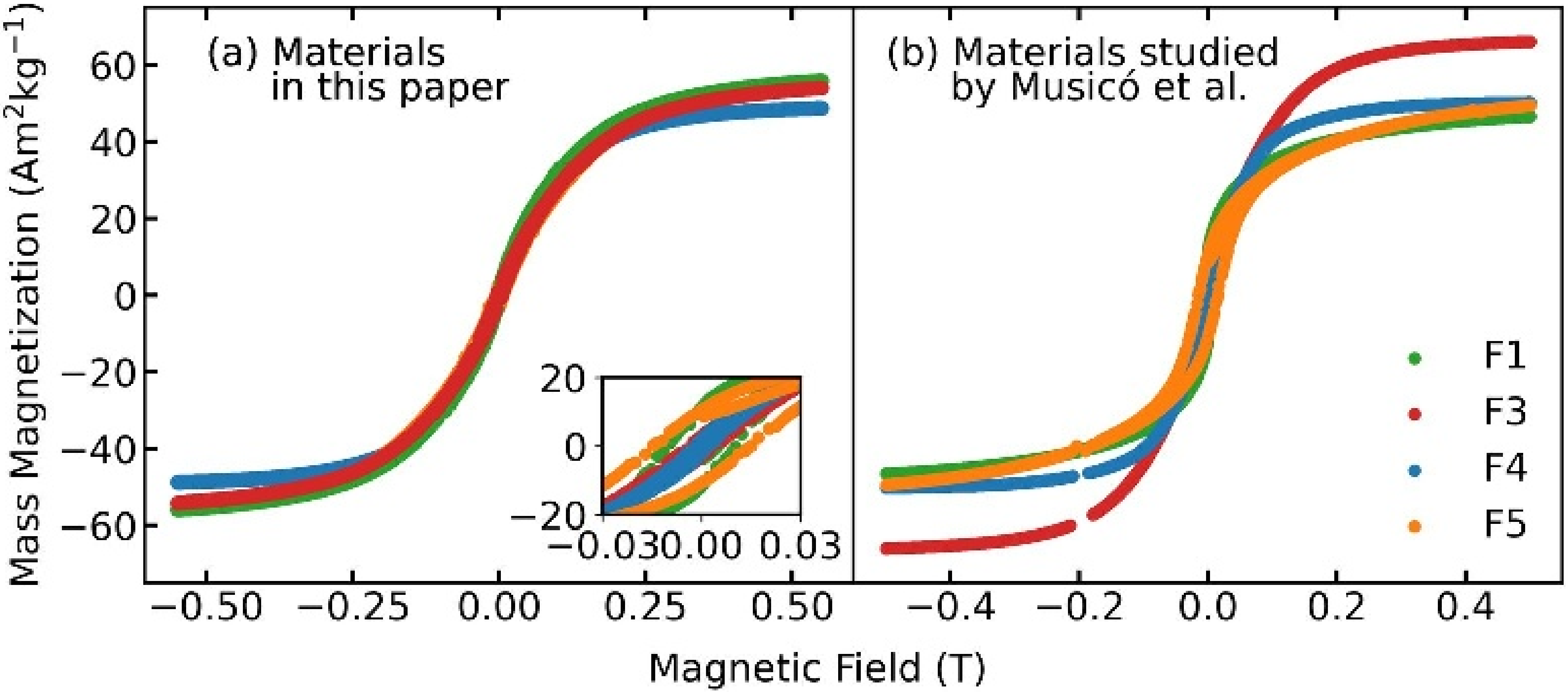
(a) Materials in this paper
(b) Materials studied by Musicó et al.
Mass Magnetization (Am²kg⁻¹)
60
40
20
0
−20
−40
−60
−0.50
−0.25
0.00
0.25
0.50
−0.4
−0.2
0.0
0.2
0.4
Magnetic Field (T)
20
0
−20
−0.03
0.00
0.03
F1
F3
F4
F5

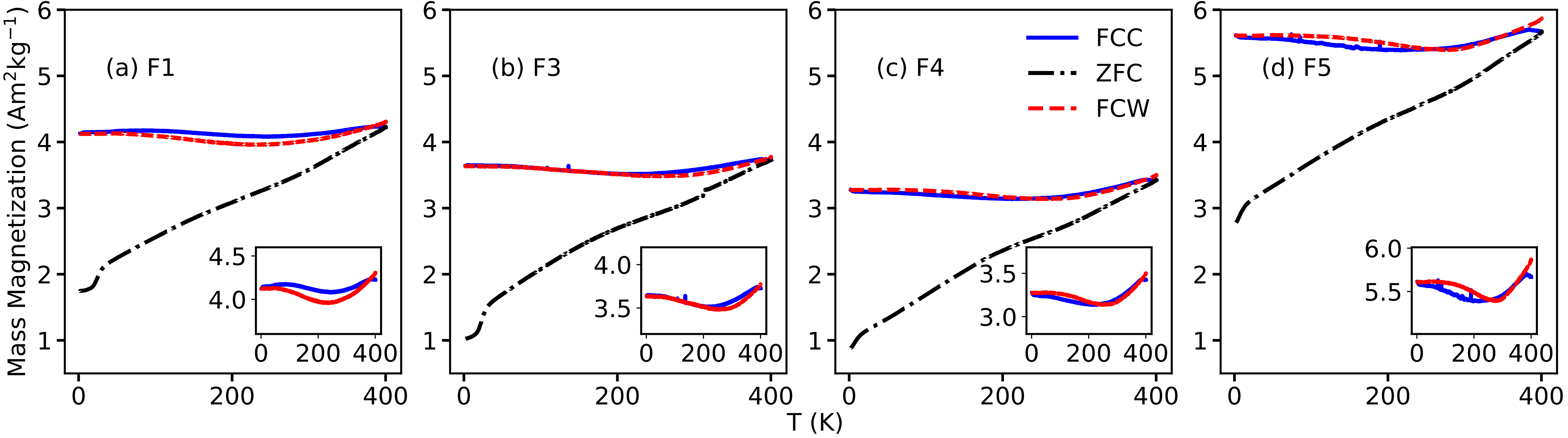
Mass Magnetization (Am^{2}kg^{-1})
T (K)
(a) F1
(b) F3
(c) F4
(d) F5
FCC
ZFC
FCW
1
2
3
4
5
6
0
200
400
4.5
4.0
3.5
3.0
5.5
6.0

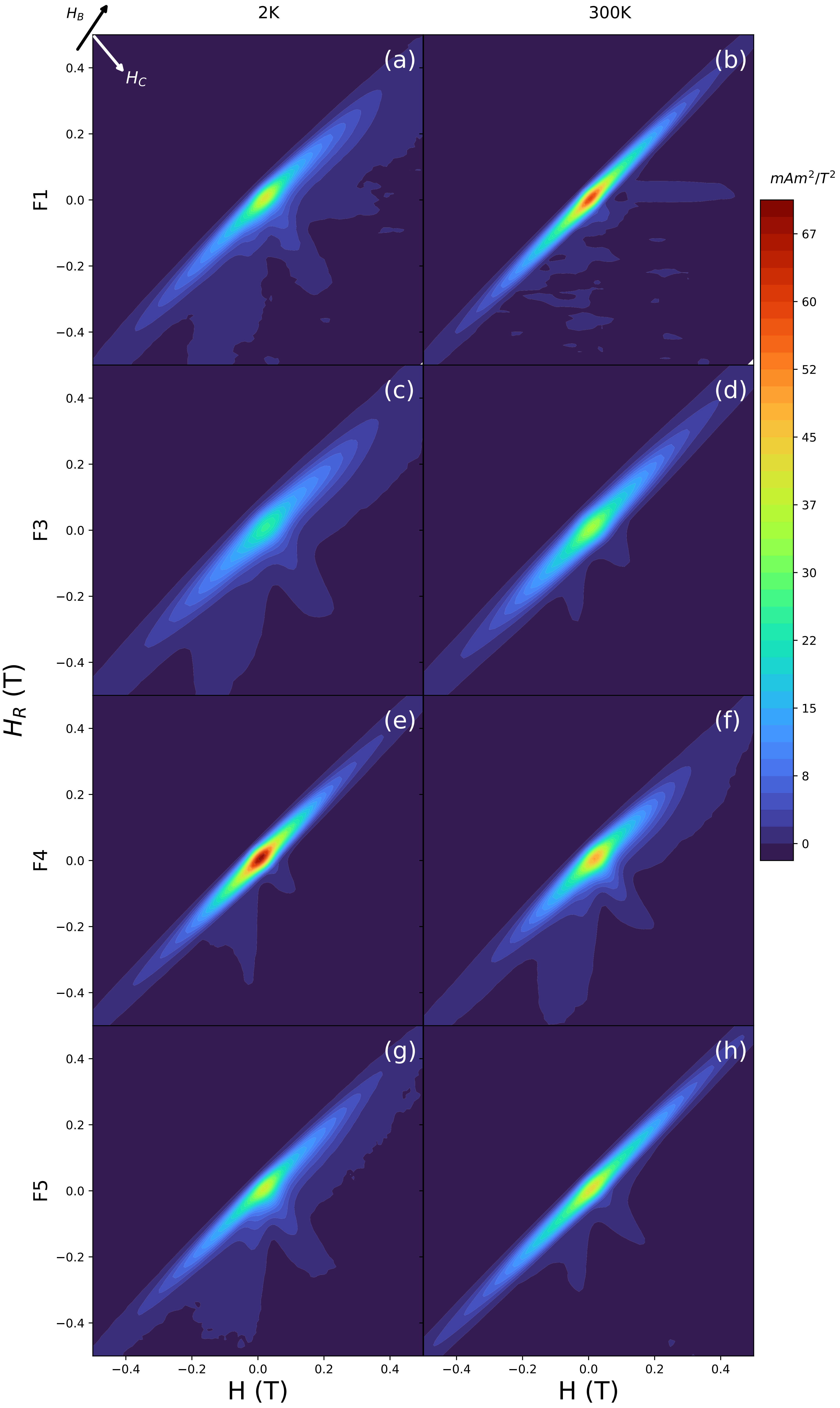
H_B
H_C
2K
300K
(a)
(b)
(c)
(d)
(e)
(f)
(g)
(h)
F1
F3
F4
F5
H_R (T)
H (T)
H (T)
0.4
0.2
0.0
−0.2
−0.4
mAm^2/T^2
67
60
52
45
37
30
22
15
8
0

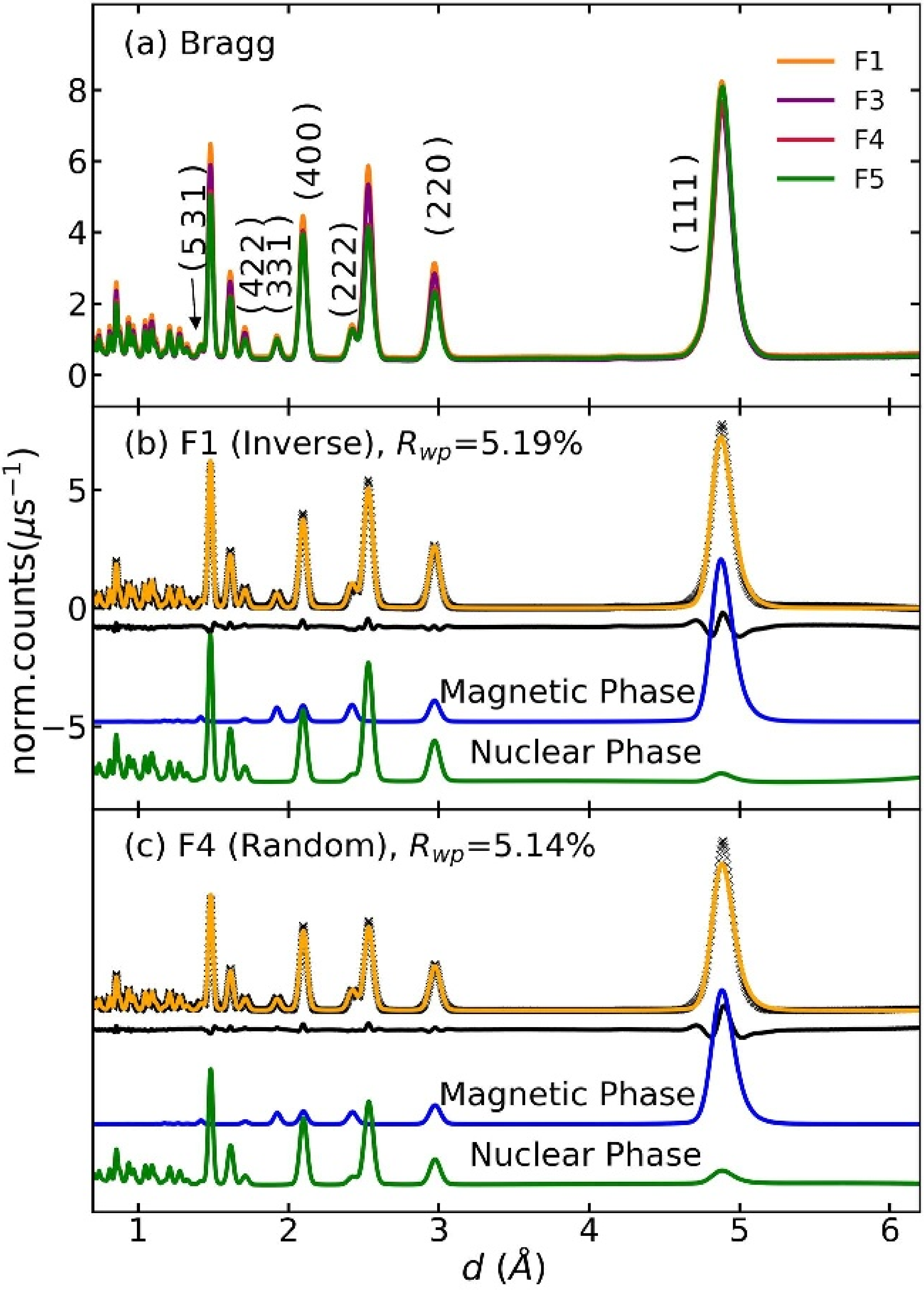
(a) Bragg
F1
F3
F4
F5
(531)
(422)
(331)
(400)
(222)
(220)
(111)
(b) F1 (Inverse), R_{wp}=5.19%
Magnetic Phase
Nuclear Phase
(c) F4 (Random), R_{wp}=5.14%
Magnetic Phase
Nuclear Phase
norm.counts(μs^{-1})
d (Å)
0
2
4
6
8
5
0
−5
1
2
3
4
5
6

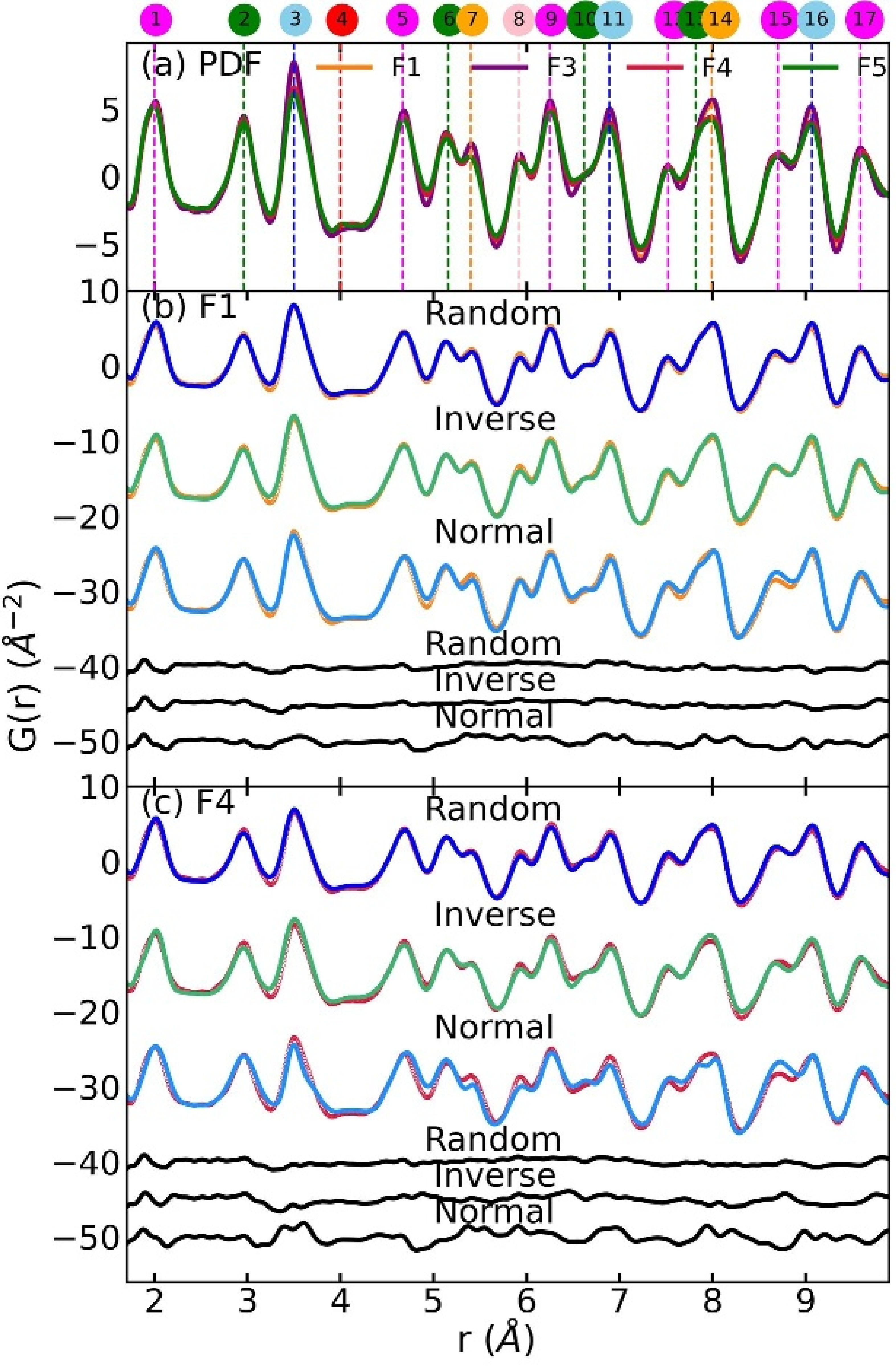
1
2
3
4
5
6
7
8
9
10
11
14
15
16
17
(a) PDF
F1
F3
F4
F5
(b) F1
Random
Inverse
Normal
Random
Inverse
Normal
(c) F4
Random
Inverse
Normal
Random
Inverse
Normal
G(r) ($\AA^{-2}$)
r ($\AA$)
10
5
0
−5
−10
−20
−30
−40
−50
2
3
4
5
6
7
8
9

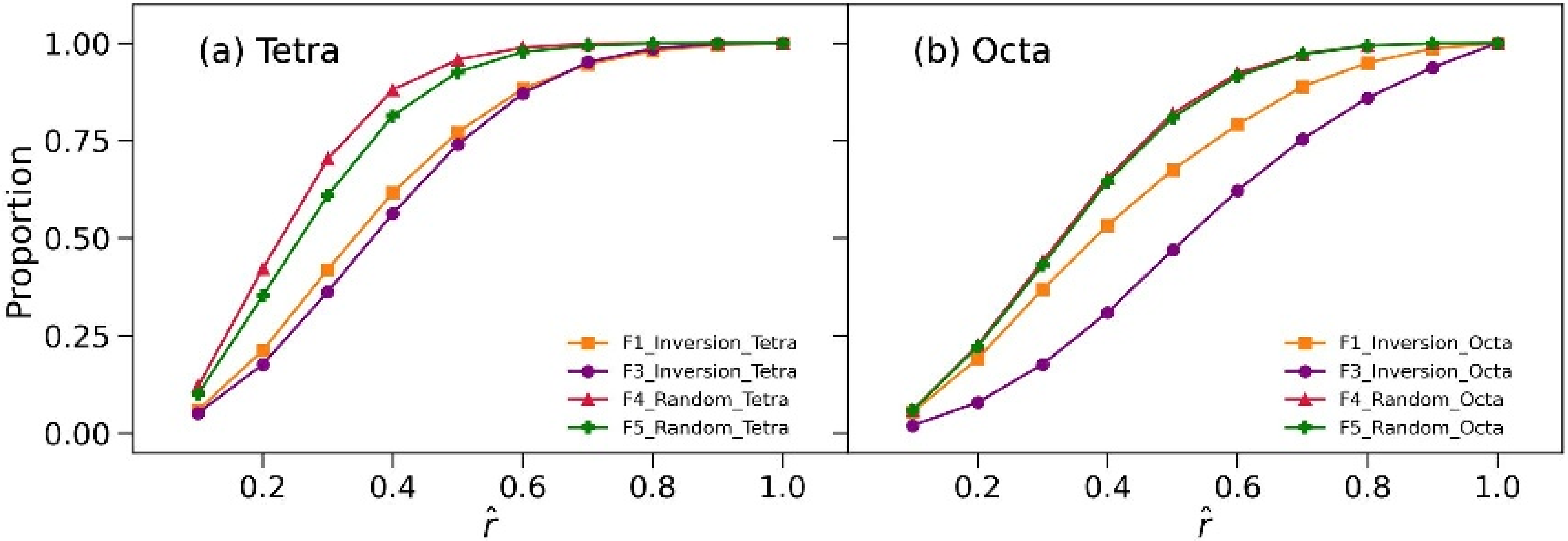
(a) Tetra
(b) Octa
Proportion
1.00
0.75
0.50
0.25
0.00
0.2
0.4
0.6
0.8
1.0
$\hat{r}$
F1_Inversion_Tetra
F3_Inversion_Tetra
F4_Random_Tetra
F5_Random_Tetra
F1_Inversion_Octa
F3_Inversion_Octa
F4_Random_Octa
F5_Random_Octa

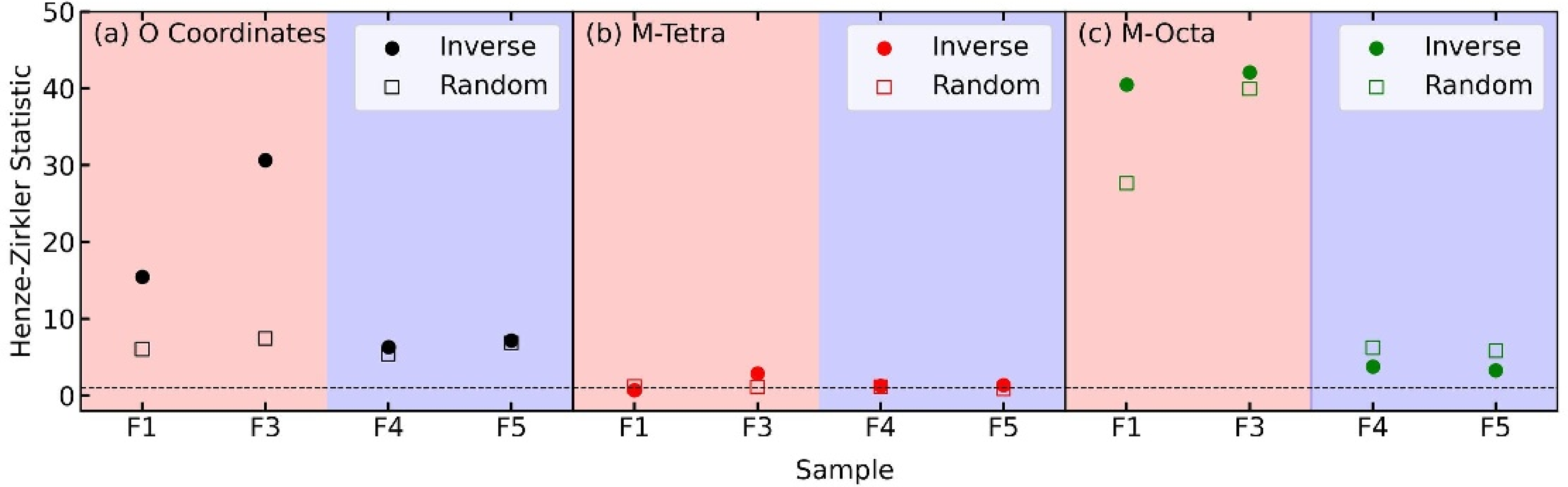
(a) O Coordinates
(b) M-Tetra
(c) M-Octa
● Inverse
□ Random
Henze-Zirkler Statistic
0
10
20
30
40
50
F1
F3
F4
F5
Sample